ARTICLES

Search for nearly massless, weakly coupled particles by optical techniques

R. Cameron,* G. Cantatore,† A. C. Melissinos, G. Ruoso,‡ and Y. Semertzidis§
Department of Physics and Astronomy, University of Rochester, Rochester, New York 14627

H. J. Halama, D. M. Lazarus, and A. G. Prodell
Brookhaven National Laboratory, Upton, New York, 11973

F. Nezrick
Fermi National Accelerator Laboratory, Batavia, Illinois 60510

C. Rizzo and E. Zavattini
Dipartimento di Fisica, University of Trieste and Istituto Nazionale di Fisica Nucleare Sezione di Trieste, 34127 Trieste, Italy
(Received 5 October 1992)

We have searched for light scalar and/or pseudoscalar particles that couple to two photons by studying the propagation of a laser beam ($\lambda=514$ nm) through a transverse magnetic field. A limit of 3.5×10^{-10} rad was set on a possible optical rotation of the beam polarization for an effective path length of 2.2 km in a 3.25 T magnetic field. We find that the coupling $g_{\alpha\gamma\gamma}<3.6\times10^{-7}$ GeV^{-1} at the 95% confidence level, provided $m_a<10^{-3}$ eV. Similar limits can be set from the absence of ellipticity in the transmitted beam. We also searched for photon regeneration in a magnetic field and found the limit $g_{\alpha\gamma\gamma}<6.7\times10^{-7}$ GeV^{-1} for the same range of particle mass.

PACS number(s): 14.80.Gt, 12.20.Fv, 14.80.Am

I. INTRODUCTION

Currently, all known particles can be accommodated in the standard model. However, the spontaneous breaking of a global symmetry implies the existence of a corresponding light neutral boson [1]. Such particles couple to two photons through the anomalous part of the triangle graph shown in Fig. 1(a), and thus can be produced by photons propagating in a static magnetic field through the Primakoff effect [2] shown in Fig. 1(b). If such particles exist, they must be coupled very weakly to matter [and thus to the electromagnetic (em) field] to have escaped detection. As a typical example, we consider the axion. The axion arises from the breaking of the U(1) Peccei-Quinn (PQ) symmetry, introduced to explain the absence of *CP* violation in QCD [3].

Considering the pions as the Nambu-Goldstone bosons associated with the breaking of chiral SU(2) symmetry, the mass m_a and symmetry-breaking scale $f_{\rm PQ}$ of the axion are related to those of the neutral pion through

$$m_a f_{\rm PQ}=N\frac{\sqrt{z}}{1+z}m_\pi f_\pi \ . \tag{1}$$

In Eq. (1), $f_\pi=93$ MeV is the pion decay constant, N is

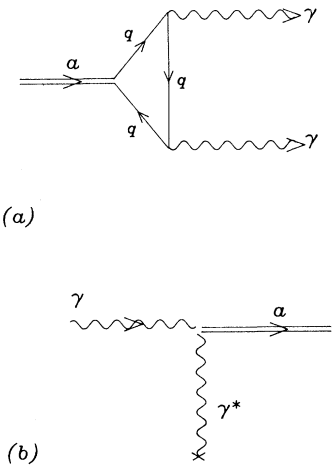

FIG. 1. (a) Axion coupling to two photons through a triangle graph. (b) Axion production by a photon propagating in a static magnetic field (Primakoff effect).

*Present address: Department of Physics, University of Western Ontario, London, ON N6A 3K7, Canada.

†Present address: Dipartimento di Fisica dell'Universita di Trieste 34127, Trieste, Italy.

‡Present address: Dipartimento di Fisica "Galileo Galilei" dell'Università di Padova, 1-35100 Padova, Italy.

§Present address: Physics Department, Brookhaven National Laboratory, Upton, NY 11973.

the color anomaly of the PQ symmetry, and $z \sim 0.56$ is the ratio of the up- to down-quark masses. Originally, $f_{\rm PQ}$ was thought to be the same as the symmetry-breaking scale of the weak interaction (250 GeV) so that the axion mass would be of order 100 keV. This axion has been ruled out by particle decay and beam dump experiments [4]. However, allowing the PQ symmetry-breaking scale to become much larger than that of the weak interaction results in a particle with low mass and weak coupling to matter [5]. Models for such "invisible axions" include the Dine-Fischler-Srednicki-Zhitnitskii (DFSZ) axion [6] which couples to all fermions and the hadronic axion first introduced by Kim [7] which couples only to quarks.

For invisible axions there are no *a priori* bounds on $f_{\rm PQ}$ except that it should lie above 100 GeV and below the Planck mass, 10^{19} GeV. The coupling to two photons $g_{a\gamma\gamma}$ can be related to the symmetry-breaking scale by

$$g_{a\gamma\gamma}=\frac{\alpha}{2\pi}\frac{1}{(f_{\rm PQ}/N)}\left[\frac{E}{N}-\frac{2}{3}\frac{4+z}{1+z}\right]; \tag{2a}$$

when the expression for m_a given by Eq. (1) is used, $g_{a\gamma\gamma}$ can be related to m_a through

$$g_{a\gamma\gamma}\approx\frac{\alpha}{2\pi}\left[\frac{m_a}{0.62\ \text{eV}}\right]0.72\zeta\times10^{-7}\ \text{GeV}^{-1}, \tag{2b}$$

where ζ is given by

$$\zeta=\left[\frac{E}{N}-1.95\right]\frac{1}{0.72}. \tag{2c}$$

Here E is the electromagnetic anomaly of the PQ symmetry and the ratio E/N is model dependent. In the DFSZ model, as well as in all models where the axion is embedded in a grand unified theory (GUT), $E/N=8/3$ leading to $\zeta=1$. Equation (2b) is not exact because of the uncertainties inherent in Eq. (1).

Low-mass axions are constrained by astrophysical arguments as extensively discussed in the reviews by Kim [8], Turner [9], and Raffelt [10]. Furthermore, very low-mass axions ($m_a \sim 10^{-5}$ eV) are considered as candidates for the dark matter in the Universe. This had led to specialized experiments to detect cosmic axions which have condensed in the galaxies. These experiments [11], which are sensitive to very low values of $g_{a\gamma\gamma}$, rely on the assumption that axions form a significant component of the galactic halo.

In the present experiment we carried out a model-independent search for light scalar or pseudoscalar particles that couple to two photons as indicated in Fig. 1(a). This was achieved by propagating a laser beam, $\omega=2.41$ eV, through a transverse magnetic field, $B\simeq3.25$ T. If the particle mass m_a is less than the photon energy ω physical particles can be produced, according to the graph of Fig. 1(b); in practice, for the length of our magnetic-field region of 880 cm, coherent production will occur only for $m_a<10^{-3}$ eV. Production of virtual particles is shown in Fig. 2(a) and manifests itself as a retardation (phase shift) of one component of polarization of the photon beam. Both of these processes are of order $g_{a\gamma\gamma}^2$.

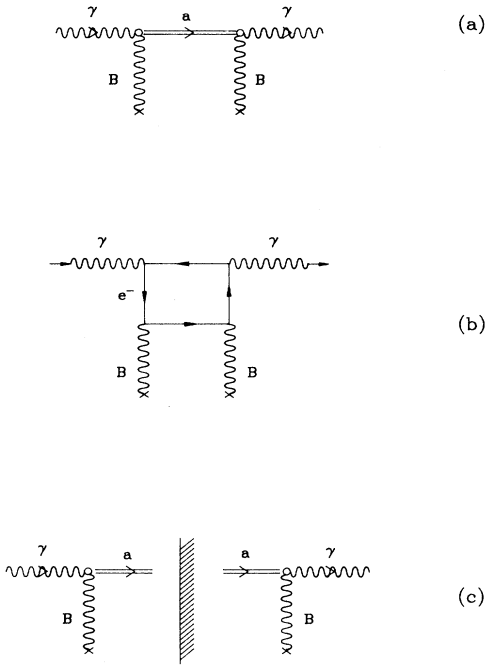

FIG. 2. (a) Virtual axion production leading to vacuum birefringence; (b) Delbruck scattering; (c) photon regeneration.

Delbruck scattering [12], shown in Fig. 2(b), also invokes the production of virtual particles but involves the well-established e-e-γ vertex. Finally, when $m_a<\omega$ it is possible to observe regeneration of photons [13] as shown in Fig. 2(c). There are also other mechanisms that can lead to photon regeneration [14]; in general, these processes are of order $g_{a\gamma\gamma}^4$.

The experimental signature for these effects can be understood as follows. A laser beam propagates through a transverse magnetic field. The external field must be transverse to avoid azimuthal symmetry. A photon is a spin-1 particle, while an axion is spin 0, and the two cannot mix in a region where azimuthal symmetry prevails. A transverse electric field could also supply the virtual photons but high-field densities are more easily achieved with a magnetic field. For coherent axion production to take place the axion and photon fields must remain in phase over the length of the magnetic field, which imposes a limit on the mass of the axions that can be detected.

We write the Lagrangian density for the interaction as

$$L=\frac{1}{4M}F_{\mu\nu}\tilde{F}^{\mu\nu}a, \tag{3a}$$

where $F_{\mu\nu}$ is the electromagnetic field tensor, $\tilde{F}_{\mu\nu}$ its dual, a is the axion field, and M is the inverse coupling constant,

$$M\equiv\frac{1}{g_{a\gamma\gamma}}, \tag{3b}$$

which has dimensions of energy. For a static magnetic field and real photons, Eq. (3a) reduces to

$$L=\frac{1}{M}(\mathbf{E}\cdot\mathbf{B}_{\rm ext})a \ .$$

Here E is the electric field of the laser beam and therefore only light polarized parallel to $\mathbf{B}_{\rm ext}$ produces axions. If the laser beam enters the magnetic-field region linearly polarized at 45° to the magnetic-field direction, the parallel component is attenuated while the orthogonal component is unaffected. The electric-field vector of the light leaving the magnetic-field region is rotated by a small angle ε, as indicated in Fig. 3(a). If the axion combines with a virtual photon to reconvert to the original photon, there is no rotation but the parallel component of the light oscillates to a massive axion for part of its travel, and so is retarded with respect to the orthogonal component. The retardation appears as an ellipticity ψ of the emerging light beam as indicated schematically in Fig. 3(b). In a similar manner, Delbruck scattering gives rise to an ellipticity in the propagated photon beam. To detect the regeneration of axions an absorber is placed between the magnets as shown in Fig. 3(c). Since the photons do not propagate through the absorber but the axions do, any photon detected at the exit of the second magnet must have been regenerated by the axion flux or by another mechanism.

In the case of a scalar particle coupling to two photons, the interaction is written as

$$L=\frac{1}{4M_s}F_{\mu\nu}F^{\mu\nu}\phi_s$$

and gives rise to similar observable effects except that it is now the component of polarization perpendicular to the magnetic field that interacts. In this experiment it was possible to measure an optical rotation as small as 3.5×10^{-10} rad, but no signal was observed. The Delbruck scattering for our apparatus results in an ellipticity of 10^{-12} rad and therefore remained beyond our detection limit.

In the next section we discuss the equations for the propagation of a photon in a magnetic field with a coupling such as shown in Fig. 1(a), and we will estimate the magnitude of the observable effects. Section III is devoted to a description of the apparatus and of the details of the experiment. In Sec. IV we discuss the sensitivity of the experiment, the sources of noise and the method of calibration. Section V contains the results obtained in terms of optical rotation and birefringence of the laser beam propagating through the magnetic field. Section VI describes the photon regeneration experiment and our conclusions are presented in Sec. VII.

II. PROPAGATION OF A PHOTON IN A MAGNETIC FIELD

The Lagrangian of a pseudoscalar particle in an electromagnetic field is

$$L=-\frac{1}{4}F_{\mu\nu}F^{\mu\nu}+\frac{1}{2}(\partial_\mu a\,\partial^\mu a-m_a^2a^2)+\frac{1}{4M}F_{\mu\nu}\tilde{F}^{\mu\nu}a \tag{4}$$

where $F_{\mu\nu}$ is the sum of the contributions from the external magnetic field and the field of real photons

$$F_{\mu\nu}=F_{\mu\nu}^{\rm ext}+\partial_\mu A_\nu-\partial_\nu A_\mu \ . \tag{5}$$

The resulting equations of motion to first order in the photon field **A** and the axion field a are

$$(\Box+m_a^2)a-\frac{1}{M}\dot{\mathbf{A}}\cdot\mathbf{B}_{\rm ext}=0 \ ,$$
$$\Box\mathbf{A}+\frac{1}{M}\dot{a}\,\mathbf{B}_{\rm ext}=0 \ , \tag{6}$$

where the gauge condition $\nabla\cdot\mathbf{A}=0$ is used, along with $A^0=0$ (the external field is transverse).

An elegant solution of these equations has been given by Raffelt and Stodolsky [15] which we include here for

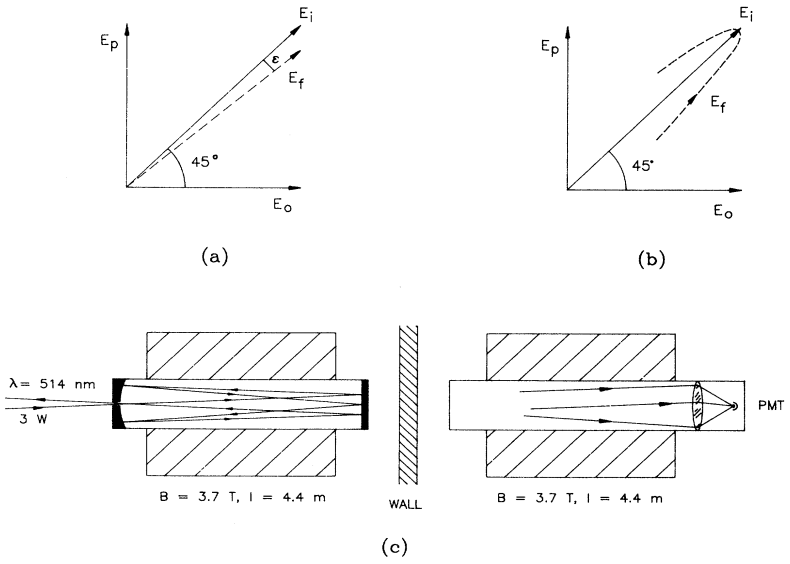

FIG. 3. (a) Optical rotation due to selective attenuation of one polarization component. (b) Elliplicity due to selective retardation of one polarization component; the dashed curve shows the locus of E_f. (c) Layout of the photon regeneration experiment.

completeness. Assuming for the fields plane-wave solutions of the form $\exp[i(\omega t - kz)]$, the coupled equations (6) can be written in matrix form

$$\begin{bmatrix} \omega^2+\partial_z^2 & 0 & 0 \\ 0 & \omega^2+\partial_z^2 & -iB_{\rm ext}\omega/M \\ 0 & +iB_{\rm ext}\omega/M & \omega^2+\partial_z^2-m^2 \end{bmatrix} \begin{bmatrix} A_o \\ A_p \\ a \end{bmatrix} = 0 , \quad (7)$$

where A_o and A_p are the components orthogonal and parallel to the external magnetic field $B_{\rm ext}$.

The external field is assumed to be very slowly varying in space and time with respect to the photon frequency so that

$$\omega^2+\partial_z^2=(\omega+i\partial_z)(\omega-i\partial_z) \approx(\omega+k)(\omega-i\partial_z)\approx 2\omega(\omega-i\partial_z) . \quad (8)$$

Thus the matrix equation for the two coupled components takes the form

$$\left[\begin{bmatrix} \omega-i\partial_z & 0 \\ 0 & \omega-i\partial_z \end{bmatrix} + \begin{bmatrix} 0 & -i\Delta_M \\ +i\Delta_M & \Delta_a \end{bmatrix} \right] \begin{bmatrix} A_p \\ a \end{bmatrix} = 0 , \quad (9a)$$

where

$$\Delta_M=\frac{B_{\rm ext}}{2M}, \quad \Delta_a=-\frac{m_a^2}{2\omega} . \quad (9b)$$

The matrix in Eq. (9a) can be diagonalized by rotating the original fields through a mixing angle θ, where θ is defined by

$$\tan 2\theta=\frac{2\Delta_M}{-\Delta_a}=\frac{2B_{\rm ext}\omega}{Mm_a^2} . \quad (9c)$$

Since the mixing is weak, $\frac{1}{2}\tan 2\theta\sim\theta$. Using this assumption, the phase shift and attenuation of $A_p(z)$ are found to be

$$\phi=\theta^2\left[\frac{m_a^2 z}{2\omega}-\sin\left[\frac{m_a^2 z}{2\omega}\right]\right]$$

and (10)

$$\delta=2\theta^2\sin^2\left[\frac{m_a^2 z}{4\omega}\right] .$$

The physical parameters that are measured are the ellipticity ψ and rotation ε, of the photon beam, which, for light entering the magnetic-field region polarized at an angle of 45° to the magnetic field, are half the phase shift and attenuation, respectively. The dependence of ψ and ε on the angle of polarization is $\sin 2\varphi$, with φ the angle between the electric-field vector of the light and the external magnetic field. Introducing Eq. (9c) in Eq. (10), the ellipticity ψ and rotation ε for light polarized at 45° reduces to

$$\psi=\frac{1}{2}\left[\frac{B_{\rm ext}^2\omega^2}{M^2m_a^4}\right]\left[\frac{m_a^2 l}{2\omega}-\sin\left[\frac{m_a^2 l}{2\omega}\right]\right] \approx\frac{(B_{\rm ext}m_a)^2 l^3}{96\omega M^2} , \quad (11a)$$

$$\varepsilon=\left[\frac{B_{\rm ext}^2\omega^2}{M^2m_a^4}\right]\sin^2\left[\frac{m_a^2 l}{4\omega}\right]\approx\frac{B_{\rm ext}^2 l^2}{16M^2} , \quad (11b)$$

where l is the length of the magnetic-field region. The probability of conversion from a photon to an axion can be found from the off-diagonal elements of the same matrix equation. The probability of conversion is

$$P_{\gamma\to a}=4\frac{B_{\rm ext}^2\omega^2}{M^2m_a^4}\sin^2\left[\frac{m_a^2 l}{4\omega}\right]\cong\frac{B_{\rm ext}^2 l^2}{4M^2} . \quad (12)$$

The approximate expressions in Eqs. (11) and (12) follow from expanding the sine and thus are valid only in the limit $m_a^2 l/4\omega\ll 1$. Therefore, for a given length l of the magnetic-field region,

$$m_a^2<2\pi\omega/l , \quad (13)$$

to preserve the relative phase between the axion and photon fields. The effective length of the magnetic-field region can be increased by multiply reflecting the laser beam through the magnets. However, since axions do not reflect, coherence is lost at every reflection. The rotation and ellipticity are cumulative upon reflection, so that for N reflections the values of ψ and ε given in Eqs. (11) are increased by a factor of N.

Polarized light propagating through a transverse magnetic field will gain an ellipticity due to Delbruck scattering. For photon energies $\omega<2m_e$, this effect is referred to as the QED vacuum birefringence and it is derived from the Lagrangian density of the electromagnetic field. To second order this can be written as [16]

$$L=-\frac{1}{4}F_{\mu\nu}F^{\mu\nu}+\frac{\alpha^2}{90m_e^4}\left[(F_{\mu\nu}F^{\mu\nu})^2+\frac{7}{4}(F_{\mu\nu}\tilde{F}^{\mu\nu})^2\right] . \quad (14)$$

The resulting ellipticity for a path length l is

$$\psi=\frac{3\alpha^2 B_{\rm ext}^2 l\omega}{45m_e^4}\sin 2\varphi \quad (15)$$

and increases linearly with the number of reflections, N. Vacuum birefringence is interesting because it is a test of QED perturbation theory at higher orders but has not as yet been measured with real incident photons. Delbruck scattering, however, has been measured in the electric field of a nucleus [17], where it appears as a small contribution to the scattering cross section and indirectly as a small contribution to the muon $(g-2)$ value, in agreement with experiment [18].

The rate for photon regeneration can be directly evaluated from Eq. (12). Light enters the magnetic-field region polarized parallel to the external field, and the counting rate of the detector due to the regeneration of photons is

$$R=(P_{\gamma\to a})^2\left[\frac{P_l}{\omega}\right]\eta\ , \tag{16a}$$

where P_l is the laser power, ω is the photon energy, and η the detector efficiency. If the light is made to pass N times through the first magnet then the counting rate is multiplied by $N/2$, since only the axions traveling in the forward direction contribute. With this factor, and using Eq. (12), the expected counting rate is

$$R=\frac{1}{16}\left[\frac{B_{\rm ext}l}{M}\right]^4\frac{N}{2}\left[\frac{P_l}{\omega}\right]\eta\ . \tag{16b}$$

By rotating the polarization of the light 90°, so that it is orthogonal to the magnetic-field direction, one can search for light scalar particles.

Photon regeneration may also take place in the absence of a magnetic field, according to Ref. [14]. The photon of the electromagnetic field is replaced by two photons (paraphotons), one of which is massive. In this case the Lagrangian for the electromagnetic field is

$$L=-\tfrac{1}{4}F_{1\mu\nu}F_1^{\mu\nu}-\tfrac{1}{4}F_{2\mu\nu}F_2^{\mu\nu}+\tfrac{1}{2}m_1^2A_{1\mu}A_1^{\mu}+\tfrac{1}{2}m_2^2A_{2\mu}A_2^{\mu}+j_\mu(e_1A_1^{\mu}+e_2A_2^{\mu})\ , \tag{17a}$$

with the photons A_1 and A_2 having masses m_1 and m_2 and coupling e_1 and e_2. Then there exist two states: the ordinary photon, which is the interacting state $\gamma=(e_1A_1+e_2A_2)/e$ and the noninteracting state $\gamma_s=(-e_2A_1+e_1A_2)/e$, where $e^2=e_1^2+e_2^2$. Oscillations can occur between the two states, so that a photon field may contain a noninteracting component that would pass through an absorber. The interacting component would be regained through oscillation on the other side of the absorber. No external field is required for the oscillation to occur.

A_1 is assumed to be the dominant component of γ, so that $m_1\sim 0$ and $m_2\gg m_1$. The mixing is then characterized by m_2 and the mixing angle θ, where $\sin\theta=e_2/e_1$. In the limit $m_1/m_2\ll 1$ and $\sin\theta\ll 1$, the conversion probability for the transition from γ to γ_s is given by

$$P_{\gamma\to\gamma_s}=4\frac{e_1^2e_2^2}{e^2}\sin^2\frac{m_2^2l}{4\omega}=\frac{l^2}{16\omega^2}m_2^4\sin^2 2\theta\ . \tag{17b}$$

The energy of the interacting photon is ω, and l is the distance the light propagates. Assuming an equal distance on the other side of the absorber, the counting rate is

$$R=\frac{(N/2)}{256}\frac{l^4}{\omega^4}\frac{P_l}{\omega}\eta(m_2^4\sin^2 2\theta)^2\ . \tag{17c}$$

As in the case of the axions, the heavy photons are not reflected by the mirrors so that the effect is linear and not quadratic in the number of reflections, N [19].

It is of interest to evaluate numerically the magnitude of the expected effects for the parameters of the experimental apparatus. All equations have been expressed in natural Heaviside-Lorentz units so that the magnetic field is given by 1 T=195 eV^2 and length by 1 m=5×10^6 eV^{-1}. The magnetic field used in the experiment was sinusoidally modulated from 2.63 to 3.87 T yielding an effective value of $B^2=4.5$ T^2. The length of the two magnets was 8.8 m, the number of reflections was $N=250$ and the photon energy $\omega=2.41$ eV. From Eq. (15) the QED vacuum birefringence for these parameters is

$$\psi=N\frac{3\alpha^2B_{\rm ext}^2l\omega}{45m_e^4}=0.22\times10^{-12}\ . \tag{18a}$$

Operating the apparatus at optimum noise performance for an integration time of $\sim$180 days leads to measurements at the 10^{-12} level.

Similarly, a rotation angle of 10^{-12} rad for the parameters of the apparatus corresponds to a limit on inverse axion coupling of

$$M>\left[\frac{NB_{\rm ext}^2l^2}{16\varepsilon}\right]^{1/2}=0.68\times10^8\ \text{GeV}\ , \tag{18b}$$

valid for

$$m_a<\left[\frac{4\pi\omega}{l}\right]^{1/2}=8\times10^{-4}\ \text{eV}\ . \tag{18c}$$

III. EXPERIMENTAL TECHNIQUE

The experimental apparatus divides naturally into two parts; the magnetic-field region, where the axions are produced, and the ellipsometer, where the resulting polarization change was measured, as shown in Fig. 4. The ellipsometer consists of two crossed polarizers (polarizer and analyzer). The input polarizer is set at 45° to the direction of the magnetic field (vertical) whereas the analyzer is oriented at 90° with respect to polarizer. In the presence of a signal the polarization of the beam would be rotated by a small angle ε before reaching the analyzer. Therefore the intensity transmitted by the analyzer is

$$I=I_0[\sigma^2+(\alpha+\varepsilon)^2]\ , \tag{19a}$$

where I_0 is the intensity incident on the analyzer, α is the misalignment angle between the polarizer and the analyzer (typically $<10^{-4}$ rad), ε is the small angle to be measured, and σ^2 is the extinction factor. For our polarizers [20], a typical extinction factor was 2×10^{-8}.

Since ε is a very small angle ($\sim10^{-10}$ rad), it is essential that the transmitted intensity contain a term that is linear in ε, rather than only the quadratic term of Eq. (19a). This was achieved by introducing a much larger, time-dependent rotation with which the desired effect mixes. A Faraday cell, consisting of a piece of borosilicate crown (BK7) glass placed inside a small solenoid coil, was introduced into the path of the transmitted light before the analyzer. It was modulated at a frequency $\omega_f/2\pi=312.5$ Hz and contributed a sinusoidal rotation of magnitude $\eta\sim10^{-3}$ rad. The transmitted intensity then has the form

$$\begin{aligned}I&=I_0\{\sigma^2+[\alpha+\eta\cos(\omega_ft+\phi_f)+\varepsilon]^2\}\\&=I_0\{\sigma^2+\tfrac{1}{2}\eta^2[1+\cos(2\omega_ft+2\phi_f)]\\&\quad+2\alpha\eta\cos(\omega_ft+\phi_f)+2\varepsilon\eta\cos(\omega_ft+\phi_f)\}\ ,\end{aligned} \tag{19b}$$

where only terms linear in ε and α have been retained.

The Faraday cell was also used for a dynamic correction of the polarizer misalignment. Because of heating and mechanical vibrations, the misalignment angle of the polarizers slowly drifts. To correct it, instead of rotating the analyzer, the polarization of the light was rotated by applying a dc voltage to the Faraday coil. The computer corrected the misalignment every 11 min at the end of each data file.

So far we have discussed only the measurement of optical rotation. However, it is also desired to measure the ellipticity induced by the beam. This was achieved in a separate measurement where a $\lambda/4$ plate was introduced in the light path before the Faraday cell as shown in Fig. 4. When properly oriented, the $\lambda/4$ plate converts the ellipticity to a rotation which can then mix with the Faraday rotation to yield a detectable signal through the analyzer.

The magnetic field was supplied by two superconducting dipole magnets. The magnets, which were prototypes for the Colliding Beam Accelerator [21], were designed to give a vertical field of 5 T when held at 4.7 K. The available cryogenic system could cool only to a temperature of 5.2 K, allowing operation at a maximum dc field of 4 T. Insulating vacuum separated the helium cooled coils from the warm bore of the magnets, which has a diameter of 3.75 in.; the magnetic-field region was 4.4 m long for each magnet.

The magnets were modulated at a frequency of 32 mHz ($\omega_m/2\pi$) between 2.63 and 3.87 T, the modulation amplitude and frequency being determined by the current ramping rate, which had to be kept below 90 A/s to prevent quenching [22]. The rotation and ellipticity are proportional to B^2, but, since the field modulation was given by

$$B = B_0 + B_\Delta \cos(\omega_m t + \phi_m) , \tag{20a}$$

with $B_0 = 3.25$ T, $B_\Delta = 0.62$ T, the dominant time-dependent B^2 term appears at frequency ω_m, and

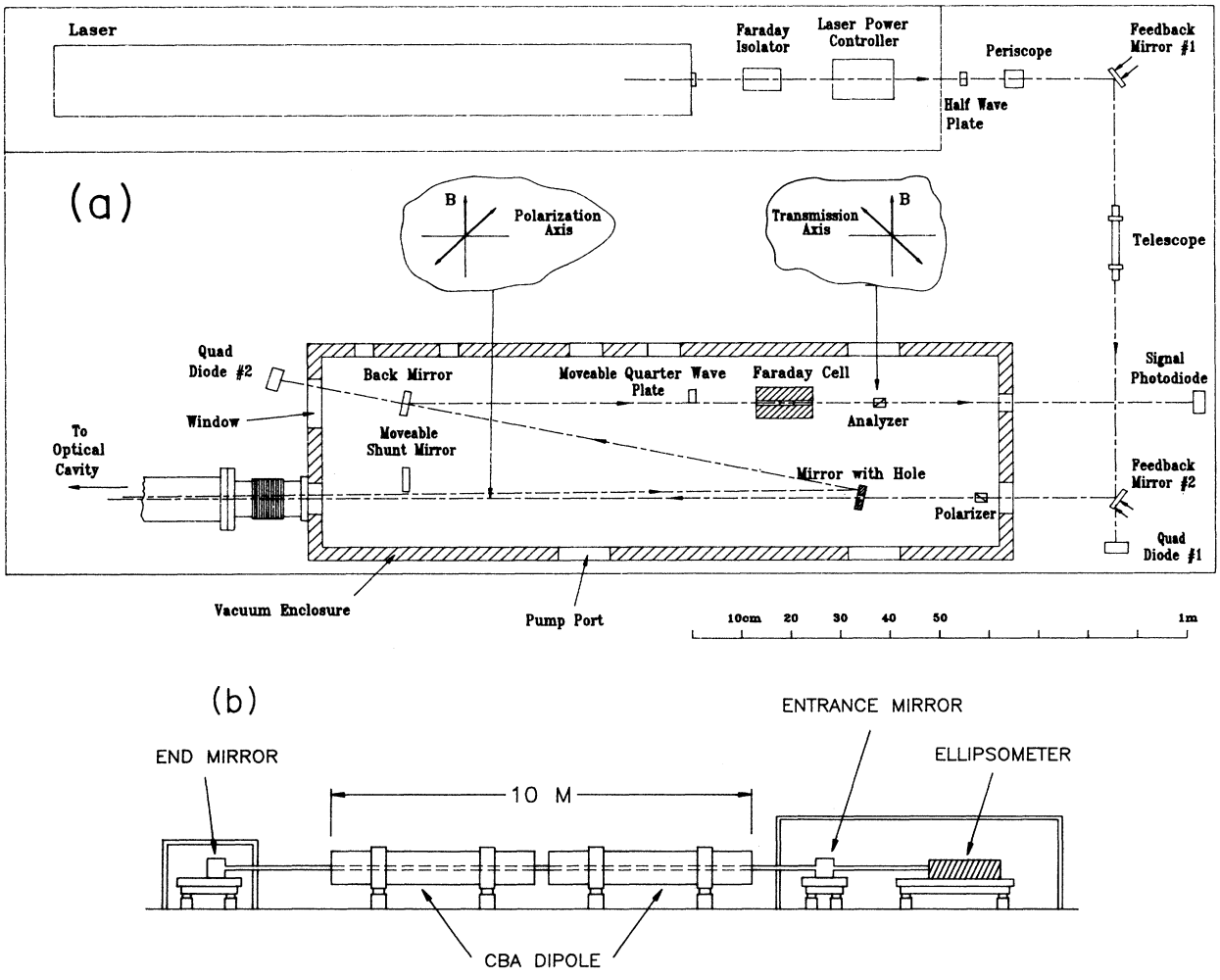

FIG. 4. (a) Schematic view of the ellipsometer; the volume inside the hatched area is evacuated. (b) Layout of the experiment and of the superconducting magnets.

$$\varepsilon, \psi \propto 2B_0 B_\Delta \cos(\omega_m t + \phi_m) \ . \tag{20b}$$

The phase ϕ_m of the magnetic field was measured to be $-176° \pm 4°$, with reference to the magnet trigger.

To obtain the longest possible light path inside the magnetic-field region, a delay line optical cavity [23], consisting of two coaxial spherical mirrors placed at either end of the magnets, was used. Light entered through a hole in the first mirror, was reflected a few hundred times between the two mirrors and then exited through the same hole. The reflectivity of the mirrors was measured to be 99.8%.

Figure 5(a) shows a typical delay line cavity. The radius of curvature R of the mirrors, and the distance between the mirrors, D_m, were chosen to satisfy the condition

$$2n\zeta = 2m\pi \ , \tag{21a}$$

where $2n = N$ is the number of trips through the cavity, m is an integer, and the angle ζ is defined by

$$\cos\zeta = 1 - D_m / R \ . \tag{21b}$$

For a stable cavity, $D_m / R < 2$. It follows that the $2n$th ray will return to the center of the mirror, and, in the absence of the hole, would repeat the pattern; in the presence of the hole the beam exits the cavity. For the case of a central hole, the pattern of spots formed on the mirror is a straight line, and the exit ray is the complement of the entrance ray. The radius of curvature of the mirrors used in the experiment was 20.53 m, and the mirrors were placed 14.9 m apart. From Eqs. (21) we obtain a basic pattern with $n = 17$, $m = 7$; that is, the light makes 34 trips through the magnetic-field region. To increase the number of reflections, one mirror was deformed along one axis, slightly increasing R for that orientation. The reflections on the cavity mirrors then formed a Lissajous pattern before exiting the cavity. Figure 5(b) shows a computer simulation of the reflections on the entrance mirror. The exact number of traversals through the cavity was determined by measuring the time delay of a short pulse of light injected into the cavity.

A telescope was used to match the waist and radius of curvature of the Gaussian beam to the lowest-order mode of the cavity. The waist of the cavity is at its midpoint, and the waist diameter was 2.5 mm; this gave a beam diameter of 3.2 mm on the mirrors. Data were acquired with two different cavity entrance mirrors with holes of 7 and 9 mm diam. The profile of the beam after exiting through the 7 mm hole (Fig. 6) showed only little diffraction; the mirror with the 9 mm hole gave no improvement, because the mirror was slightly astigmatic. Because the light reflects from the cavity mirrors several hundred times, any static birefringence due to the mirrors can become large. To control this, the birefringent axes of each mirror were found and the mirrors were mounted so that the axis was aligned with the polarization of the light.

The cavity volume was pumped by three ion pumps and was maintained at 10^{-7} Torr since gas in the magnetic-field region would induce an ellipticity due to the Cotton-Mouton effect. The box containing the ellipsometer was held at 10^{-6} Torr by a turbo pump, the two vacuum regions being connected by a 1.5-in.-diam tube that could also be pumped by an axial ion pump.

The laser used in the experiment was an argon-ion laser made by Coherent. The laser was capable of producing 5 W when running at all lines, but was operated at a single line at 514.5 nm where up to 2 W could be delivered. To avoid noise due to thermal stress in the optics, we operated at a level of 0.5 W. The laser was used in the transverse electromagnetic (TEM_{00}) mode, where the specifications for the laser beam were radius 0.75 mm and divergence 0.5 mrad at the output coupler, which is 140 cm from the laser beam waist. In addition to the light regulation of the laser itself, we used an external laser power controller (LPC) [24]. The LPC had a stated

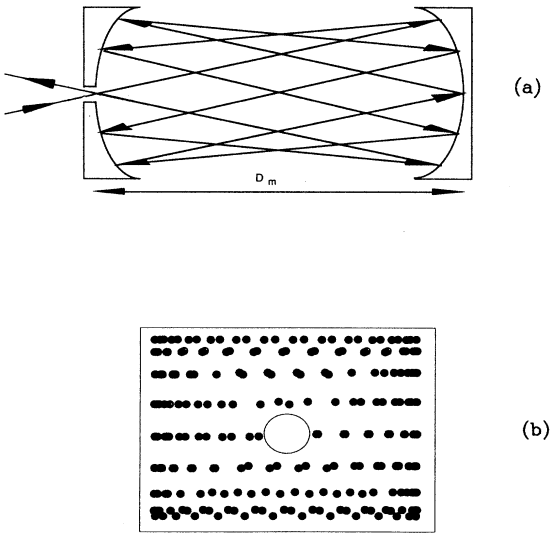

FIG. 5. (a) Delay line optical cavity for $n = 5$, $m = 1$. (b) Calculated impact points on the end mirror for a cavity with 460 traversals.

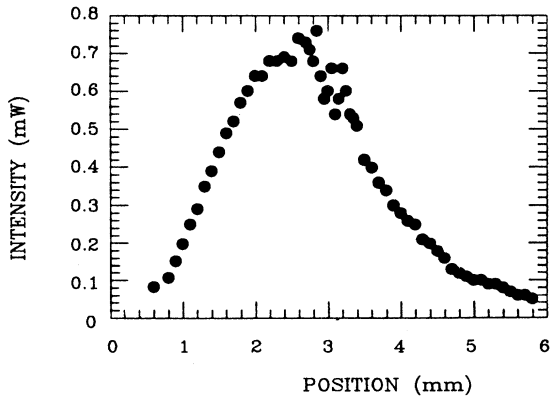

FIG. 6. Profile (one dimensional) of the laser beam after exiting the multipass optical cavity through a 7 mm hole. The slight asymmetry is due to "clipping" of the Gaussian tails.

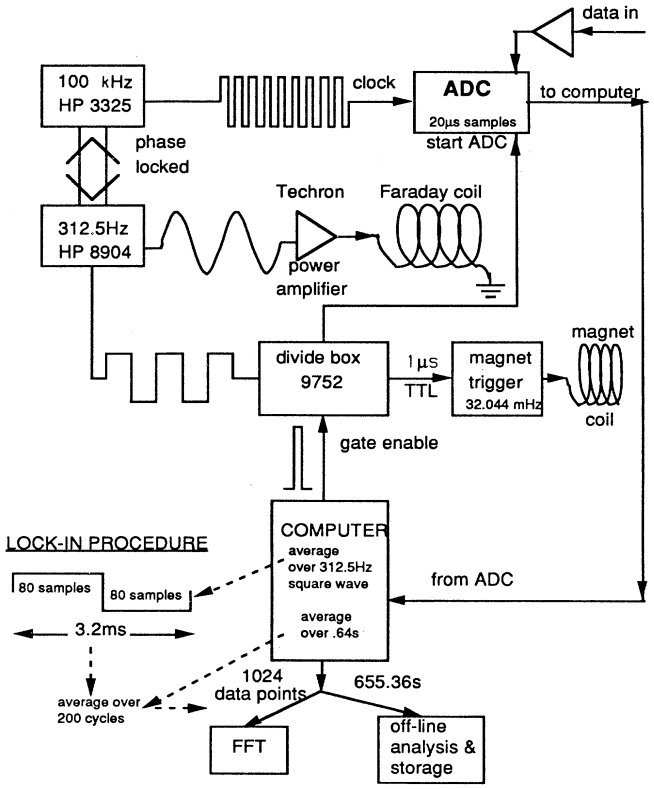

FIG. 7. Flowchart of the data acquisition system.

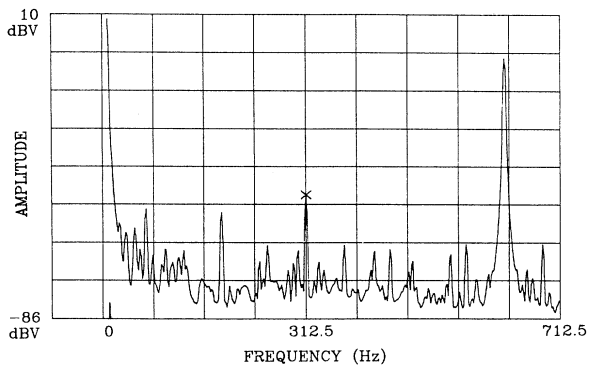

FIG. 8. Frequency spectrum of the signal showing the dominant lines at: dc, $\omega_f/2\pi=312.5$ Hz and $2\omega_f/2\pi=625$ Hz.

long-term power stability of 0.05% and optical noise reduction of 40:1; with the LPC placed after the laser we achieved an overall noise reduction factor of 2.

The Faraday cell voltage was supplied by two channels of a four channel synthesizer, Hewlett Packard (HP) 8904. Channel 1 supplied a 312.5 Hz sine wave, 4 V peak to peak; channel 2 supplied the dc offset used for the misalignment correction which was of order 10 mV. The resulting signal was amplified to about 10 V by a power amplifier and used to drive the Faraday cell coil. The amplified voltage was chosen such that

$$\tfrac{1}{2}\eta^2=\sigma^2 \tag{22}$$

which optimized the signal to noise ratio as discussed in Sec. IV. The third channel of the synthesizer provided a 312.5 Hz square wave, which was scaled by 9752 to give a transistor-transistor logic (TTL) signal at 32.044 mHz, which in turn triggered the magnet. The magnet trigger, Faraday cell voltage, and data acquisition clock were phase locked together.

The light transmitted through the analyzer was detected by a silicon photodiode. The signal was amplified by a current sensitive preamplifier with adjustable gain, usually operated at a gain of 10^8 V/A. This signal, now on the order of 1 V, was sent to a differential filter that suppressed everything outside the frequency band 310–315 Hz. This was necessary to avoid dynamic range problems by removing the large signals at 625 Hz ($2\omega_f/2\pi$) and at dc. The small signal within this narrow frequency band was then amplified to a level of 1 or 2 V and sent to a 16-bit analogue-to-digital converter (ADC) card, which digitized the filter output, and directly transmitted it to the computer. A flow diagram of the electronics is shown in Fig. 7.

The time base for the data acquisition was a 100 kHz square-wave external clock generated by an HP 3325 synthesizer referenced to the HP 8904. The ADC converted data at a rate of 50 kHz, the conversion being initiated by the magnet trigger. It was possible to view the entire frequency spectrum on an HP 35660A analyzer as shown in Fig. 8. The frequency band from 0 to 712.5 Hz was displayed so that the dc light level, misalignment, and Faraday signal could be monitored. The spectrum analyzer was controlled by the computer via the Hewlett Packard Interface Bus (HPIB) and the amplitudes of these three signals were stored with each data file.

To detect the signal of interest, the light intensity incident on the photodiode was Fourier analyzed, as described above, for a frequency component at the magnet modulation frequency, $\omega_m/2\pi$. Since the photodiode current was also strongly modulated at the Faraday cell frequency $\omega_f/2\pi$, the signal appears as a sideband at $\omega_f\pm\omega_m$. The relevant terms in the frequency spectrum of the transmitted light are

$$I=I_0(\sigma^2+\tfrac{1}{2}\eta^2+2\alpha\eta\cos(\omega_f t+\phi_f)$$
$$+\varepsilon\eta\{\cos[(\omega_f+\omega_m)t+\phi_f+\phi_m]+\cos[(\omega_f-\omega_m)t+\phi_f-\phi_m]\}+\tfrac{1}{2}\eta^2\cos(2\omega_f t+2\phi_f))\ . \tag{23}$$

To provide sufficient frequency resolution and dynamic range, a spectral analysis system was built, based on the 16-bit ADC card, which transferred the data directly to the memory [direct memory access (DMA)] of the IBM-386 compatible computer. Figure 9 shows the flow diagram for the spectral analysis. The ADC acquired 160, 20 μs samples in 3.2 ms, which is the time period of the 312.5 Hz carrier wave. To demodulate the signal, the

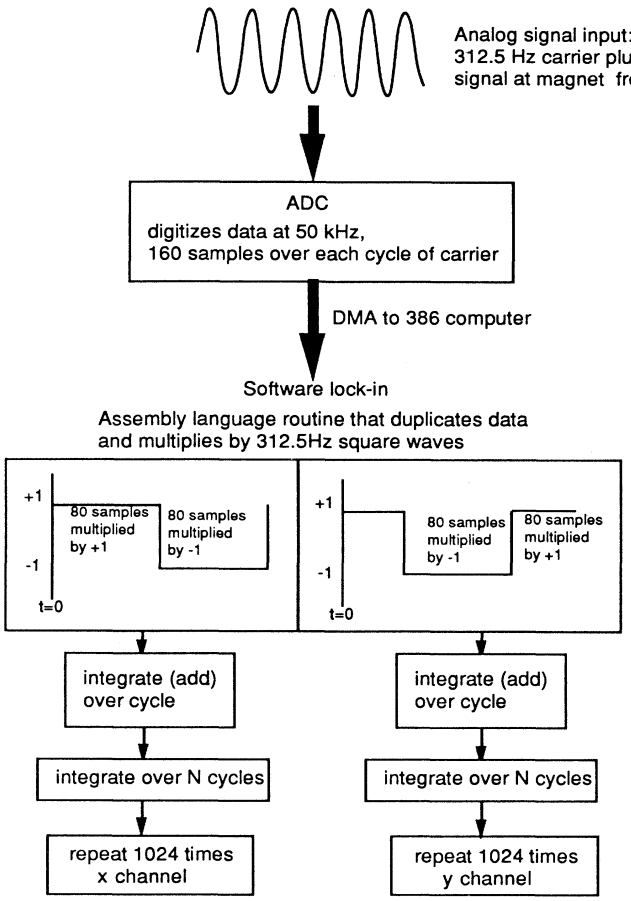

FIG. 9. Flowchart for signal processing and spectral analysis.

data stream from the ADC was multiplied by a square wave of frequency 312.5 Hz, before being integrated. This was accomplished by an assembly language routine that multiplied the data by $+1$ during the first half of the data cycle, and by -1 during the second half; the 160 numbers were then added. The software demodulation was completed by averaging the data over a chosen number of cycles; the data so collected were called the x channel; the same operation was also performed with the square wave shifted by 90°, to give the y channel so that both the phase and amplitude of each Fourier component could be determined. Thus a data file contained 1024 numbers in each channel, and each file was stored for off-line analysis while also analyzed on line.

The data file was input to a fast Fourier transform (FFT) routine which returned a frequency spectrum containing both negative and positive frequencies about 312.5 Hz. Typically, the integration time was chosen to be 655.36 s, giving a frequency resolution of 1.5258 mHz, the 512 channels covering $\pm 0.781\,25$ Hz. Table I lists the definitions used for Fourier components of the signal, and their respective magnitude and phase. The phases of the sideband signals, ϕ_+ and ϕ_-, are the sum and the difference of the Faraday cell phase and magnet phase, as measured with respect to the magnet trigger:

TABLE I. Definitions used for the spectral components of the signal.

Frequency	Fourier component	Amplitude	Phase
0	$I_{\rm dc}$	$\sigma^2+\frac{1}{2}\eta^2$	
ω_f	$I_{\omega f}$	$2\alpha\eta$	ϕ_f
$\omega_f+\omega_m$	I_{s+}	$\psi\eta$ or $\varepsilon\eta$	ϕ_+
$\omega_f-\omega_m$	I_{s-}	$\psi\eta$ or $\varepsilon\eta$	ϕ_-
$2\omega_f$	$I_{2\omega f}$	$\frac{1}{2}\eta^2$	$2\phi_f$

$$\phi_+=\phi_m+\phi_f,\quad \phi_-=\phi_m-\phi_f\ . \tag{24a}$$

Thus the magnetic-field phase and Faraday cell phase can be extracted (modulo π) from the data by adding and subtracting ϕ_+ and ϕ_-:

$$\phi_m=\tfrac{1}{2}(\phi_++\phi_-),\quad \phi_f=\tfrac{1}{2}(\phi_+-\phi_-)\ . \tag{24b}$$

If the signal is genuine the value of ϕ_m obtained from the data through Eq. (24b) must coincide with the directly measured value of $\phi_m=-176\pm4°$. In this way signals due to systematic effects in the data could be identified as discussed in Sec. V.

Knowledge of the phase of each Fourier component makes it possible to "vector average" data from several files. Namely, instead of simply averaging the magnitude of each spectral component over a number of data sets, a vector sum is carried out. This reduces the random noise in the frequency spectrum by a factor $\sqrt{n}$ where n is the number of sets averaged. In contrast, in a scalar (rms) average the random noise remains constant and only its fluctuations are reduced by $\sqrt{n}$. Because the phase of the magnetic field was known, the positive and negative frequencies could be vector averaged together, further reducing the random noise by $\sqrt{2}$.

IV. NOISE CONSIDERATIONS AND CALIBRATION

The ultimate limit in the sensitivity that can be achieved is set by the noise in the apparatus as well as by the magnitude of the effect that can be generated. The latter depends on the strength of the magnetic field and the number of traversals through the field region. The noise depends on the systematic and random motion of the beam and optics, and ultimately on the statistical fluctuations of the light reaching the detector. If the laser power exiting the cavity is 0.1 W, which corresponds to approximately $N=0.25\times10^{18}$ photons/s, then, on general grounds, the relative fluctuations in the signal after 1 s of integration will be

$$\Delta N/N=1/\sqrt{N}=2\times10^{-9}\ .$$

In what follows we will evaluate the signal-to-noise ratio in more detail, but the above estimate correctly sets the scale of the statistical noise contributions. This noise level decreases as the square root of the integration time.

Statistical fluctuations in the signal intensity are due to the random emission of electrons from the photodiode when light is incident on it (shot noise). The (rms) statist-

ical fluctuations in the current I_{dc} are given by Schottky's formula [25]

$$\delta I_s = \sqrt{2eI_{dc}/T_{int}} , \tag{25a}$$

where T_{int} is the integration time. For this experiment,

$$I_{dc} = eQ\frac{P_0}{\omega}\left[\sigma^2 + \frac{1}{2}\eta^2\right] , \tag{25b}$$

where Q is the quantum efficiency of the photodiode (0.65), and P_0 is the power incident on the analyzer, approximately 200 mW. It is useful to express the shot noise as a current density, i.e., per unit square root of bandwidth (W_B), where we defined $W_B \equiv 1/T_{int}$:

$$i_s = \frac{\delta I_s}{\sqrt{W_B}} = e\left[2Q\frac{P_0}{\omega}\left[\sigma^2 + \frac{1}{2}\eta^2\right]\right]^{1/2} . \tag{25c}$$

In addition to shot noise, the photodiode signal is affected by fluctuations in the laser intensity and laser pointing. The laser amplitude noise varies with frequency and with light power. The relative laser amplitude noise density at the Faraday cell frequency was measured in our experiment to be

$$\delta P/P = 10^{-5}/\sqrt{\text{Hz}}$$

and therefore contributes noise in the photodiode current with a density of

$$i_l = \left[\frac{\delta P}{P}\right] eQ\frac{P_0}{\omega}\left[\sigma^2 + \frac{1}{2}\eta^2\right] . \tag{26a}$$

At low light levels (i.e., good extinction) the preamplifier noise can become important. This is due to thermal fluctuations in the input impendance R_f of the amplifier

$$i_j = \sqrt{4kT/R_f} , \tag{26b}$$

which predicts $i_j = 1.3\times10^{-14}$ A/$\sqrt{\text{Hz}}$ for $R_f = 10^8$ Ω. The preamplifier used in the experiment had a measured noise current density of 3×10^{-14} A/$\sqrt{\text{Hz}}$ when operated on the $R_f = 10^8$ scale, namely, two and a half times the thermal limit. The contribution of these three noise sources is shown in Fig. 10 as a function of the relative dc amplitude $I_{dc}/I_0 = (\sigma^2 + \frac{1}{2}\eta^2)$ for $P_0 = 0.2W$, $Q = 0.65$, and $\lambda = 514.5$ nm. Typically, the experiment was operated in the region of $\sigma^2 + \frac{1}{2}\eta^2 \sim 10^{-7}$.

For an optical rotation ε, the signal light intensity is $\varepsilon\eta I_0$ [see Eq. (23)] and therefore the signal-to-noise ratio (S/N) for the shot-noise limited case is

$$S/N = \frac{\varepsilon\eta\sqrt{QP_0/\omega}}{2\sqrt{\sigma^2 + \frac{1}{2}\eta^2}}\sqrt{T_{int}} . \tag{27a}$$

(Here we used peak rather than rms shot noise which introduces a further factor of $\sqrt{2}$.) To improve the S/N in this case it is desirable to have $\frac{1}{2}\eta^2 > \sigma^2$ and when $\frac{1}{2}\eta^2 = \sigma^2$

$$S/N = (\varepsilon/2)(\sqrt{QP_0/\omega})\sqrt{T_{int}} . \tag{27b}$$

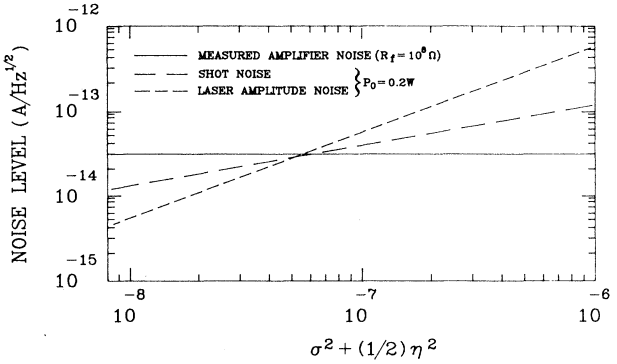

FIG. 10. Shot noise, amplifier noise, and laser amplitude noise densities plotted against the relative dc amplitude $I_{dc}/I_0 = [\sigma^2 + \frac{1}{2}\eta^2]$. The shot noise and laser amplitude noise have been calculated for $P_0 = 0.2$ W and $\delta P/P = 10^{-5}/\sqrt{\text{Hz}}$; the amplifier noise is the measured figure at $R_f = 10^8$ Ω.

The value of S/N improves only by $\sqrt{2}$ as $\eta^2 \gg \sigma^2$. As is evident from Eqs. (26) the laser and amplifier noise also scale as $1/\sqrt{T_{int}}$. Equation (27b) can be inverted to give (S), the sensitivity of the system, expressed as a rotation density. Taking $S/N = 1$ and $P_0 = 0.2$ W, $Q = 0.65$, $\lambda = 514.5$ nm as before, we find

$$S = 4\times10^{-9} \text{ rad}/\sqrt{\text{Hz}} \tag{27c}$$

at the shot-noise limit. Namely, to reach a rotation level of 10^{-10} rad (with $S/N = 1$) it would be necessary [26] to integrate for $T_{int} = 1600$ s at optimum performance.

The source of noise most difficult to control in this experiment was due to random fluctuations in the position of the light beam and to systematic fluctuations at the magnet modulation frequency ω_m. These were caused by mechanical vibrations of the optical components and by the limited pointing stability of the laser. Because of the very delicate extinction of the beam by the crossed polarizers, any motion of the beam on the analyzer resulted in fluctuations in the transmitted intensity. We refer to this effect as misalignment noise, which became more pronounced as the laser pointing stability deteriorated during the course of the experiment. This was seen as a widening of the $1/f$ shape in the frequency spectra of the analyzed data and resulted in sensitivities for a multipass cavity of only 10^{-6} rad/$\sqrt{\text{Hz}}$. To control this problem, we constructed a feedback system using two piezoelectric controlled mirrors [27] to lock the laser beam at two well-separated positions. The laser motion in each position was monitored by a quadrant diode [28], located behind a 95% reflecting dielectric mirror. The positions of the diodes and of the piezo-controlled mirrors are shown in Fig. 4(a). The second quadrant diode monitors light which has been transmitted through the cavity, so that the second feedback mirror compensated for cavity motion as well as for the pointing instability of the laser. With this system, the fluctuations in the pointing of the laser were reduced to below 0.1 μm over a lever arm of 2 m.

Table II lists the lowest noise level (and the corre-

TABLE II. Best sensitivites achieved with the feedback system operating.

Number of reflections	Rotation or ellipticity	Number of averages	Measured rms noise level (rad)	Achieved sensitivity (rad/$\sqrt{\text{Hz}}$)
Shunt	Rotation	48	4.3×10^{-11}	7.6×10^{-9}
Shunt	Ellipticity	25	2.0×10^{-10}	2.6×10^{-8}
34	Rotation	66	1.6×10^{-10}	3.3×10^{-8}
34	Ellipticity	25	2.0×10^{-9}	7.9×10^{-8}
254	Rotation	40	4.2×10^{-10}	6.7×10^{-8}
578	Ellipticity	13	5.1×10^{-8}	1.5×10^{-6}

sponding sensitivity) achieved with the feedback system in operation as *measured* for various configurations of the apparatus. To separate the ellipsometer from the optical cavity, a "shunt mirror" could be inserted in the beam path at the location indicated in Fig. 4(a). In this configuration the laser beam that has passed through the polarizer is redirected to the analyzer, bypassing the cavity and allowing independent adjustment of the ellipsometer. Under these conditions and with the magnetic field off, the observed noise level for rotation measurements was only a factor of 2 larger than that predicted by Eq. (27c). In contrast, the ellipticity measurement is three times less sensitive because the $\lambda/4$ plate is strongly affected by beam motion. This is also true for the configurations where the cavity is used.

The remaining four entries in Table II were obtained with the beam traversing through the cavity and with the modulated magnetic field on. Now the motion of the cavity mirrors was the dominant source of noise which is seen to significantly exceed the shot noise limit and to increase with the number of reflections used. Note that the total integration time for each of the measurements reported in Table II can be obtained by multiplying the number of averages by 655 s.

It was possible to calibrate the apparatus by introducing a small amount of nitrogen into the cavity. In a region of transverse magnetic field, most gases become birefrigent. This is known as the Cotton-Mouton effect [29], where the constant C_{CM} is defined by

$$\Delta n = n_p - n_o = C_{\text{CM}} \lambda B^2 \ . \tag{28a}$$

Here n_p (n_o) is the index of refraction for light polarized parallel (orthogonal) to the external field. The ellipticity induced in the light beam is given by

$$\psi_c = \frac{\pi N l}{\lambda} \Delta n = \pi C_{\text{CM}} \sin 2\theta \int (\mathbf{B}\times\mathbf{k})^2 dx \ , \tag{28b}$$

with Nl the total optical path length, $\mathbf{k}$ the light-propagation vector, and θ the angle between $\mathbf{B}\times\mathbf{k}$ and the polarization vector of the light, the integration being carried over the length of the optical path. Nitrogen gas, which has a known C_{CM}, was used to calibrate the apparatus, and furthermore the ellipsometer was sensitive enough to also make the first ever measurements of C_{CM} of helium and neon [30,31]. The results of these measurements are given in Table III. Note that oxygen is a very dangerous contaminant for these measurements, since C_{CM} of O_2 is ten times that of N_2, and therefore the cavity must be carefully flushed if it is open to air.

The data for 100 Torr of He are shown in Fig. 11 and indicate a noise floor of 10^{-9} rad, the S/N being of order 50; the sideband signal peaks are clearly separated from the central (misalignment) peak and have the expected phase with respect to the magnet trigger. The peaks at ±170 mHz are due to a vibration at this frequency. The Cotton-Mouton effect for N_2, even at a pressure of few Torr, was so large that it could be directly recorded in

TABLE III. (a) Cotton-Mouton coefficient C_{CM} measured for N_2, Ne, and He. (b) Observed ellipticity due to the CM effect for N_2 and He.

(a)

Gas	Purity	C_{CM} at 760 Torr, 298 K (G^{-2} cm^{-1})
N_2	99.996%[a]	$(-4.4\pm0.2)\times10^{-17}$
Ne	99.995%[b]	$(5.5\pm0.3)\times10^{-20}$
He	99.999 97%[a]	$(3.2\pm0.7)\times10^{-20}$

(b)

Gas	Pressure (Torr)	ψ_{expt} (rad)	ψ_{calc} (rad)
N_2	49±0.5	$(-1.09\pm0.003)\times10^{-4}$	$(-1.07\pm0.05)\times10^{-4}$
He	98.5±0.5	$(1.65\pm0.01)\times10^{-7}$	$(1.56\pm0.34)\times10^{-7}$

[a]O_2 content less than 5 parts in 10^8, water content less than 1 part in 10^7.
[b]O_2 content less than 3 parts in 10^6, water content less than 5 parts in 10^6.

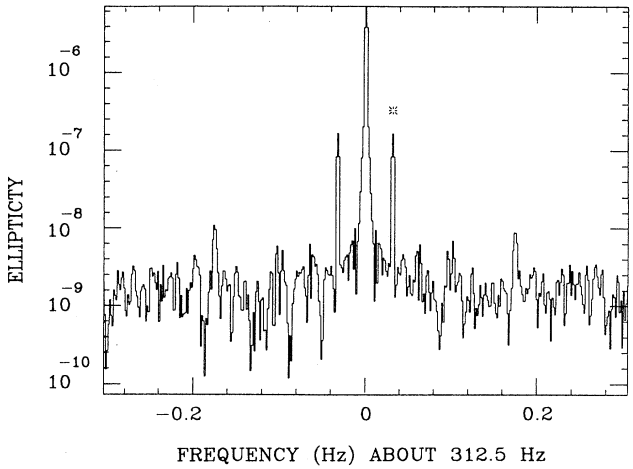

FIG. 11. The Cotton-Mouton effect for 100 Torr of helium.

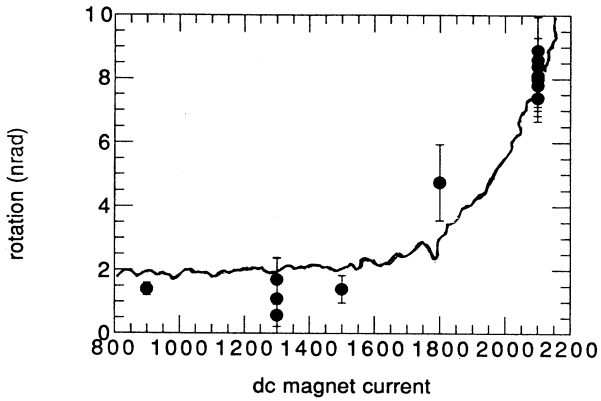

FIG. 12. Observed optical rotation as a function of the dc value of the magnet current before shielding. The curve is proportional to the measured stray magnetic field.

the time domain, without any need to Fourier analyze the data.

V. RESULTS

The production of axions would manifest itself as two sideband peaks in the power spectrum of the light reaching the detector. The sidebands would be at the Faraday cell frequency of 312.5 Hz, and would be separated from the dominant "misalignment" peak by the magnet modulation frequency of 32.044 mHz as shown for the Cotton-Mouton effect in Fig. 11. Such sidebands, however, can also be generated by systematic instrumental effects and were observed during the experiment. In most cases they can be distinguished from a genuine signal as follows: we rotate the polarization of the light parallel to the magnetic field in which configuration axion production does not result in optical rotation; thus if the sidebands persist they must be instrumental. Two primary sources of such false signals were a stray magnetic field acting on the Faraday glass and polarizers, and the motion of the cavity mirrors at the magnet modulation frequency.

First, the cavity path was blocked by inserting the shunt mirror, yet sideband peaks remained present in the spectrum. These peaks had the correct phase (same as the magnetic field), and the magnitude and phase did not vary as the light polarization was changed. The dependence of the magnitude of the peaks on B_0, the dc value of the magnetic field, is shown in Fig. 12, and is far from linear. In fact, it follows the strength of the stray field as the dipoles become saturated, as shown by the superimposed curve in Fig. 12.

The dominant effect of the stray magnetic field is Faraday rotation in the Faraday glass and the two polarizers. Considering the Faraday glass alone, the stray field necessary (along the direction of propagation of the light) to give a rotation of 8.5×10^{-9} rad is

$$B=\frac{8.5\times10^{-9}\text{ rad}}{(3.25\text{ rad/T m})\times0.254\text{ m}}=1.0\text{ mG}\ .$$

Near the laser, 0.8 mG was measured in the vertical direction and 0.5 mG along the direction of propagation of the light. The rotation due to a Faraday effect on the cavity mirrors and steering optics was measured to contribute less than 10^{-10} rad to the signal.

When the upstream end of the magnet was encased in a double layer of 0.25 in. μ metal shielding, the signals were no longer visible above a noise floor of 1.6×10^{-10} rad. Assuming the signal to be entirely due to the Faraday glass, the stray magnetic field at the Faraday cell location must have been reduced by a factor of 50, to 20 μG. Rotation data obtained with the shunt mirror in place and with the magnetic field shielded are shown in Fig. 13(a); no sidebands are apparent. Ellipticity data under the same conditions (shunt mirror in place magnetic field shielded) are shown in Fig. 13(b); small sidebands are seen because of the influence of the magnetic field on the $\lambda/4$ plate.

When the light traversed a multipass cavity, much larger signals appeared. Such signals, of magnitude 4.3×10^{-8} rad, were first observed early in the experiment [32]. Rotating the polarization parallel to the magnetic field did not eliminate them, so it was known that the peaks were not due to the production of axions. At that time, the second cavity mirror was measured with a displacement meter, and was found to move with the magnet cycle with an amplitude of 5 nm. The magnet cryostat showed much larger motion, almost 1 μm.

To damp any motion being transmitted by the beam tube to the mirrors, the mirrors were moved further from the magnets and a series of soft bellows-rigid support-soft bellows couplings was added between the magnets and the cavity mirrors. When this work was completed, mirror motion could no longer be measured with the displacement meter. However, signals of magnitude $\sim10^{-8}$ rad were still visible. That the mirrors were still moving with the magnet cycle was established by Fourier analyzing the correction signal of the feedback system; this is evident from Fig. 14 which shows the Fourier transform of the feedback correction signal for the Φ motion (horizontal plane) of feedback mirror No. 2 (see Fig. 4). The peak at the magnet frequency indicates that the feedback system is attempting to compensate for a periodic angu-

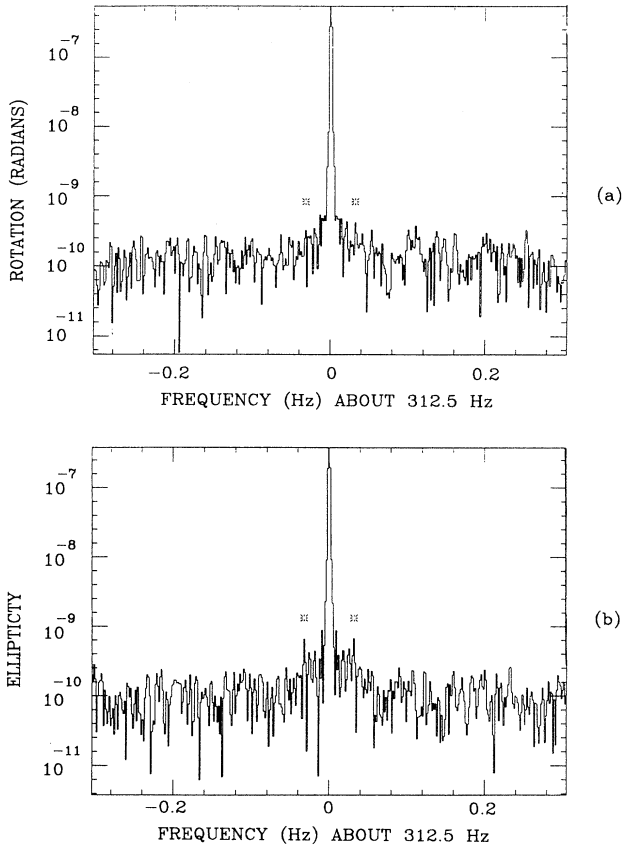

FIG. 13. Final data with shunt mirror in place: (a) rotation, (b) elliplicity.

lar displacement of the beam of magnitude 10^{-8} rad.

The signals observed in the data due to mirror motion did not remain at the same magnitude and phase for more than a few hours of data acquisition. The phase in particular was random whereas the magnitude was proportional to the path length in the multipass cavity. We infer that the mirrors were mechanically coupled to the magnet cryostats, most probably through the floor since they all rested on a single slab of concrete.

During the off-line analysis, each data file was Fourier transformed separately so that any especially noisy data files could be removed. Another criterion for rejecting a data file was an abrupt change in $I_{\rm dc}$ and $I_{2\omega f}$. Despite the feedback system, during a data run the cavity pattern could drift so that the beam scraped the hole in the cavity entrance mirror. This was manifested by a change in $I_{2\omega f}$, and caused increased misalignment noise as well as amplifying the magnitude of the false signal peaks. To avoid biasing the result, the selection of the data was based only on these two criteria, and not on the existence or absence of peaks. Several data runs, where the apparatus was in the same configuration, were combined and the data files were both rms and vector averaged. For multipass cavity data, the rms average shows larger signals than the vector average, as expected, because the peaks generated by mirror motion exhibit a random

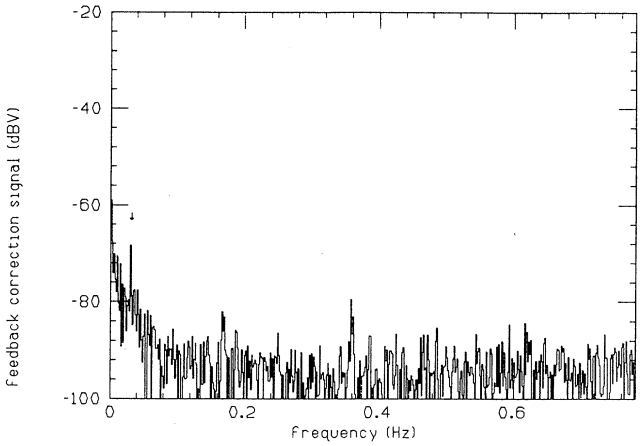

FIG. 14. Fourier transform of the correction signal for the second feedback system, Φ motion. The peak at the magnet frequency shows that the feedback system tries to correct for the cavity mirror motion.

phase.

The data obtained on the measurement of the optical rotation are summarized in Table IV(a). These are given for three configurations of the optical beam path: (a) multipass cavity with 254 reflections, (b) single ellipse cavity with 34 reflections, and (c) shunt mirror where there is no traversal through the magnetic field. All data were acquired with the light polarized at 45° to the magnetic field, and with the magnets ramped between 2.63 and 3.87 T. Both rms and vector averaged values of the signal at the magnet modulation frequency are given; background has not been subtracted from the listed values of the rotation angle. The phase given is $\frac{1}{2}(\phi_+ + \phi_-)$ (modulo π), and for a genuine signal should be exactly $4\pm4°$. This condition is satisfied by the shunt mirror data but not by the cavity data. Data sets that exhibited a peak at the magnet modulation frequency are flagged in the table by *Y* (yes) whereas the absence of a peak is indicated by *N* (no).

The results of folding the positive and negative frequency data together are presented in Table IV(b). The vector averaged data were used and the large reduction in the value of ε obtained from the multipass cavity data occurs because the phase for this data set is very close to 90° with respect to the magnet phase [33]. The 2σ level for the signal is indicated by $\varepsilon_{95\%}$ and corresponds to a 95% confidence upper limit on a possible optical rotation for these configurations. The sensitivity limit for these data sets was given in Table II. The folded data for the multipass cavity are shown in Fig. 15(a).

Using $\varepsilon_{95\%}$ from the multipass cavity, the limit on the axion coupling to two photons $g_{a\gamma\gamma} \equiv 1/M$, is calculated from Eq. (11b). This is shown in Fig. 16(a) and, for $m_a^2 \ll 2\pi\omega/l$,

$$M > \left[\frac{N(2B_0B_\Delta)L^2}{16\varepsilon_{95\%}} \right]^{1/2} = 2.8\times10^6 \text{ GeV} , \qquad (29a)$$

where we used $L = 8.8$ m, $\omega = 2.41$ eV, and $2B_0B_\Delta = 4$ T^2

TABLE IV. (a) Optical rotation measured with multipass cavity, one ellipse cavity, and shunt mirror. (b) Component of optical rotation in phase with the magnet current.

(a)

Number of reflections	Number of averages	ε_{rms} (nrad)	ε_{vec} (nrad)	Noise level (nrad)	Phase (deg)	Peak above noise
254	40	8.9	4.4	0.42	84±12	*Y*
34	66	1.7	0.36	0.16	33±14	?
shunt	22	1.0	0.37	0.21	20±20	*N*

(b)

Number of reflections	ε (nrad)	Noise level (nrad)	$\varepsilon_{95\%}$ (nrad)	Peak above noise
254	0.35	0.30	0.60	*N*
34	0.26	0.11	0.38	?
shunt	0.37	0.15	0.52	*Y*

[see Eqs. (20)]. The limit obtained from the single ellipse data is weaker, yielding $M > 1.3\times10^6$ GeV.

The same analysis procedure was used for the ellipticity data. Table V(a) shows the rms and vector averages, whereas the folded results and corresponding confidence limits are given in Table V(b). The folded data for the multipass cavity are shown in Fig. 15(b). The limit on axion coupling to two photons is calculated from Eq. (11a) from the multipass cavity using $\psi_{95\%}$:

$$M > \left\{ \frac{N}{2\psi_{95\%}} \left[\frac{2B_0 B_\Delta \omega^2}{m_a^4} \right] \left[\frac{m_a^2 L}{2\omega} - \sin\left[\frac{m_a^2 L}{2\omega} \right] \right] \right\}^{1/2} \tag{29b}$$

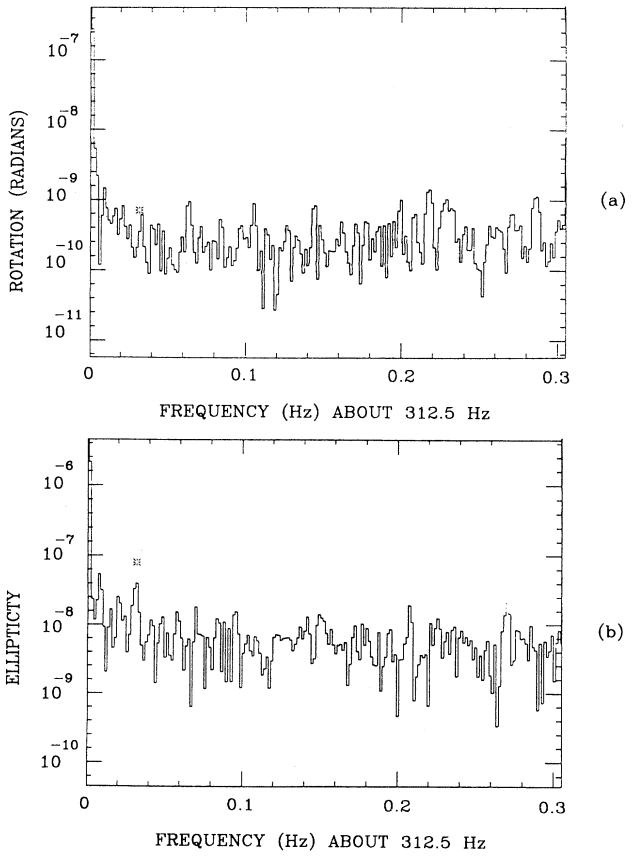

FIG. 15. (a) Folded optical rotation data for a 254 reflection cavity, (b) folded ellipticity data for a 578 reflection cavity.

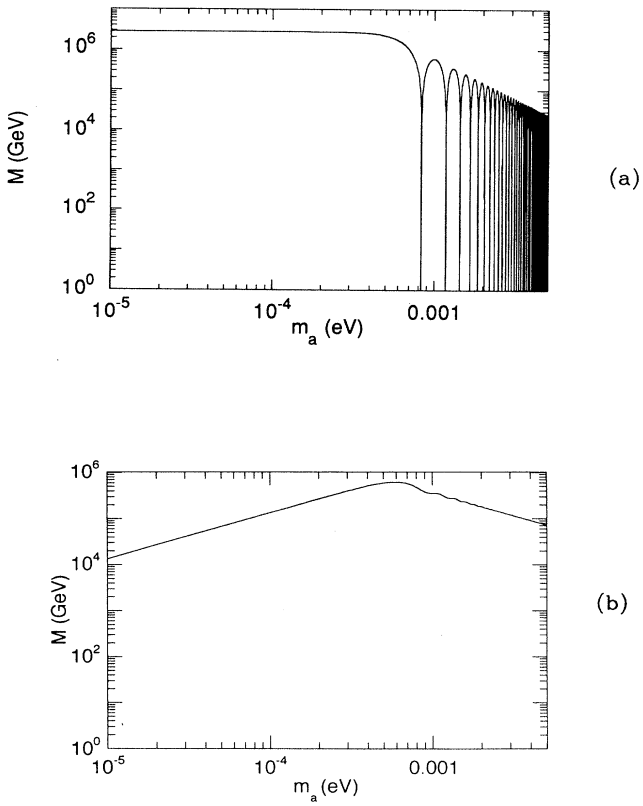

FIG. 16. Upper limits on the axion coupling to two photons ($g_{a\gamma\gamma}=1/M$). The limit on the inverse coupling M is plotted as a function of axion mass: (a) from the optical rotation data of Fig. 15(a); (b) from the ellipticity data for a 34 reflection cavity.

TABLE V. (a) Ellipticity measured with multipass cavity, one ellipse cavity and shunt mirror. (b) Components of the vacuum ellipticity in phase with the magnet current.

(a)

Number of reflections	Number of averages	ψ_{rms} (nrad)	ψ_{vec} (nrad)	Noise level (nrad)	Phase (deg)	Peak above noise
578	13	95	67	15.5	57±8	Y
34	25	5.5	2.2	0.62	40±18	Y
shunt	25	1.2	0.66	0.20	9±16	Y

(b)

Number of reflections	ψ (nrad)	Noise level (nrad)	$\psi_{95\%}$ (nrad)	Peak above noise
578	40.0	11.0	51.0	Y
34	1.6	0.44	2.0	Y
shunt	0.63	0.14	0.77	Y

and is a function of the axion mass. It is shown in Fig. 16(b). In this case we used the single ellipse data because it gives a better limit than the multipass data as can be seen in Table V(b); this is due to the large systematic effects in the multipass cavity data. While the ellipticity limit is weaker than the rotation limit for $m_a < 10^{-3}$ eV, it becomes significant for $m_a > 10^{-3}$ eV because for ellipticity, M falls off as $1/m_a$, whereas for rotation, M falls off as $1/m_a^2$ [see Eqs. (11)].

VI. PHOTON REGENERATION

The principle of the photon regeneration experiment was discussed in the Introduction and the expected counting rate is given by Eq. (16b). The experimental arrangement is shown in Fig. 3(c) with both magnets set to a dc field $B_{dc}=3.7$ T. The laser was run on all lines (principally 488 and 514.5 nm) to increase the power to 3 W. A Lissajous cavity was formed spanning only the first magnet; furthermore, the return mirror of the cavity was flat to ensure that the optical rays projected to the end of the second magnet would remain within the 3.75-in.-diam magnet aperture. The cavity was operated with 200 reflections. The polarization was set parallel to the magnetic field when searching for photon regeneration due to the production of pseudoscalar particles and perpendicular to the field for the case of scalar particle production. A rotary chopper provided a 10 Hz modulation of the laser beam, the "on" and "off" states being monitored by a photodiode.

The end of the first magnet was blocked, and so was the entrance to the second magnet. At the end of the second magnet, an $f=25$ cm lens focused any light onto the 9-mm-diam sensitive photocathode area of a 9893B/350 photomultiplier tube (PMT) manufactured by Thorn EMI. This is a special, low dark current tube which was cooled to a temperature of -23 °C. The 14 stage tube was operated at 2000 V; at this gain, the single photoelectron peak corresponded to $Q\sim 20$ pC, and the dark counting rate in the single photoelectron peak was 0.6 Hz. The quantum efficiency of the bialkali photocathode at our wavelength was $\eta=0.1$. The position and width of the single and multiple photoelectron peaks were determined by injecting light from a light emitting diode located at the upstream end of the second magnet. Figure 17 shows three such pulse height spectra, fitted with Poisson distributions for a mean number of 0.13, 1.4, and 9.7 photoelectrons, respectively.

The PMT output was split into two parts, one half of the signal being used to provide an electronic trigger. The other half of the signal was digitized by a LeCroy 2249, CAMAC controlled, charge sensitive ADC; the sensitivity was 0.25 pC/channel and the integration gate $\Delta t=100$ ns. The CAMAC crate controller communicated with a PC computer via the HPIB bus. The computer also received the signal from the photodiode which monitored the on/off state of the laser light. The dark current (no light incident on the PMT) spectrum is shown in Fig. 18(a). The large peak in the pedestal region is due to electronic noise and is clearly separated from the single photoelectron peak, shown on the expanded scale in the inset. The fit to the data is a truncated Gaussian centered at channel 108, with a standard deviation of 34 channels, as determined from the calibration. The counting rate is $R=0.6$ Hz and the $\chi^2/N_{DF}=1.27$.

The data acquisition program collected an on spectrum of events when the chopper allowed the laser beam to enter the cavity; and an off spectrum of events with no light in the cavity. To insure that equal time was spent in the on and off states, the trigger counts in the noise region below the single photoelectron peak were monitored and compared. To simulate a signal, we allowed a small amount of light to enter directly from the first, into the second magnet; in this case subtracting the off spectrum from the on spectrum resulted in the data shown in Fig. 18(b). These data were fitted by the same truncated Gaussian as in (a) of the figure, and yield $R_{on}-R_{off}=2.1$ Hz and the $\chi^2/N_{DF}=0.89$.

With no light allowed into the second magnet, the subtracted spectrum is as shown in Fig. 18(c). These data corresponded to 220 min with laser on, and to 220 min with laser off and were taken with the light polarization parallel to the magnetic field (pseudoscalars). There were

approximately 7000 counts in each state, showing no significant difference between laser on and laser off. The results of all the data, including that acquired with the light polarization orthogonal to the field (scalars) and with the magnets off (massive photons), are summarized in Table VI. The cuts on the pulse height spectrum used to select single photoelectron events introduced a further efficiency $\eta' = 0.55$.

For the parameters of the experiment the value of the inverse coupling of pseudoscalars to two photons is related to the limit on the counting rate through Eq. (16b):

$$R = (0.085 \text{ Hz}) \left[\frac{10^6 \text{ GeV}}{M} \right]^4 . \tag{30}$$

The 2σ limit on the observed rate is $R_{2\sigma} < 0.018$ Hz, and therefore

$$M > 1.5 \times 10^6 \text{ GeV} .$$

This limit is valid for $m_a < 10^{-3}$ eV, and its dependence on mass is very similar to that shown in Fig. 16(a); see Eq. (12). For more details see Ref. [34].

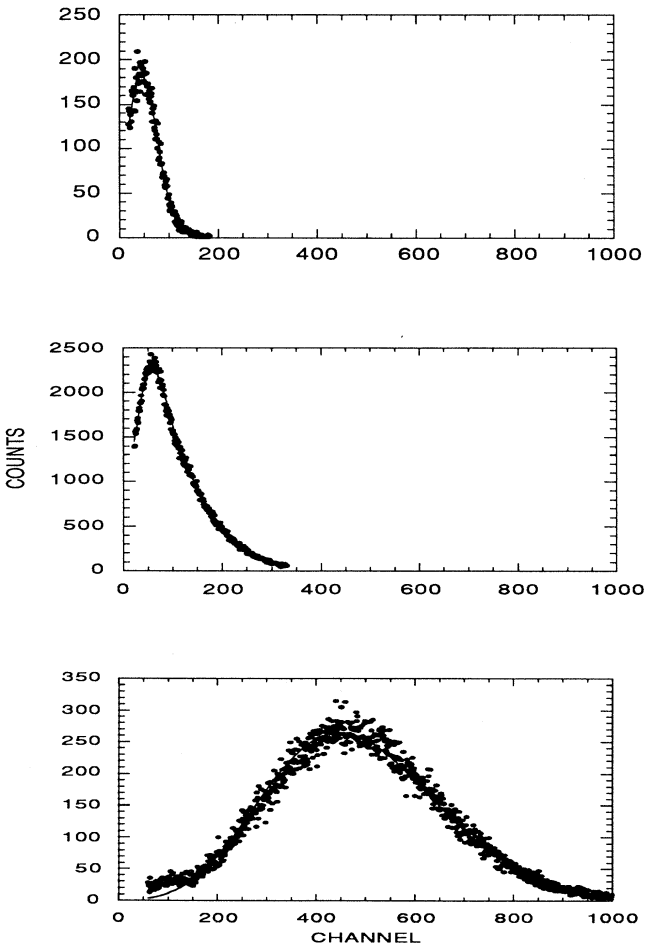

FIG. 17. Calibration spectra corresponding to a mean number of (a) 0.13, (b) 1.4, and (c) 9.7 photoelectrons.

In Sec. II we discussed a possible model of deviations from pure electrodynamics introduced in Ref. [14]. The expected regeneration rate was given by Eq. (17c) whereas experimentally the 2σ limit on the observed rate is $R_{2\sigma} < 0.004$ Hz. This sets a limit on the product of the mixing angle $\theta \sim e_2/e_1$ and heavy photon mass m_2 of

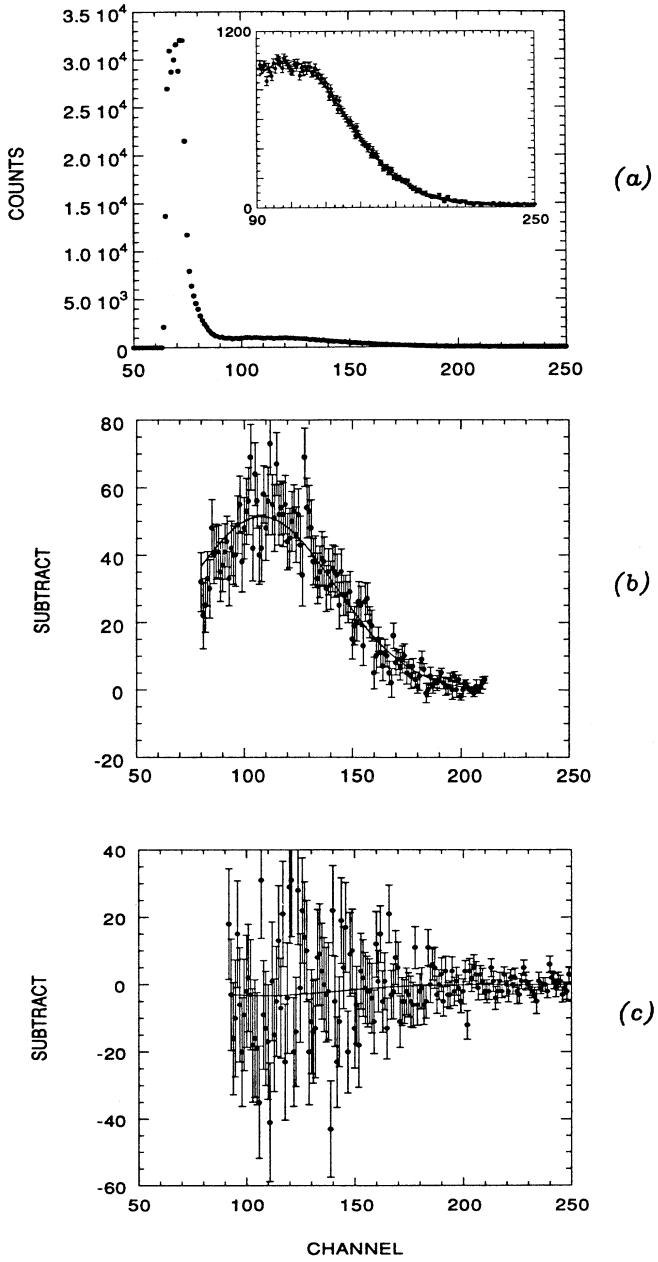

FIG. 18. Integrated charge spectrum. The pedestal is at channel 63 and the single photoelectron peak [see inset in (a)] is fitted by a truncated Gaussian centered at channel 108, with standard deviation of 34 channels. The sensitivity is 0.25 pC/channel. (a) Dark current spectrum including the electronic noise. (b) Subtracted spectrum when light was admitted from the first magnet; used for calibration. (c) Subtracted spectrum when no light was allowed into the second magnet.

TABLE VI. Summary of results from the photon regeneration experiment.

Data set	Time laser on (s)	Number of counts	Rate (Hz)	$\chi^2/N_{\rm DF}$
Pseudoscalar	13.3×10^3	-159 ± 115	-0.012 ± 0.009	1.0
Scalar	15.7×10^3	199 ± 102	0.013 ± 0.007	0.7
Massive photon	59.7×10^3	252 ± 144	0.004 ± 0.002	0.8

$$m_2^4(\sin2\theta)^2<(1.0\times10^{-6}\ \text{eV})^4\ .$$

Our limit is shown in Fig. 19, together with other limits on the existence of a massive photon.

VII. CONCLUSIONS

From the observed absence of an optical rotation [Eq. (29a)] we conclude that there exist no massless or low mass, $m_a<10^{-3}$ eV, particles that couple to two photons with a strength $g_{a\gamma\gamma}\equiv1/M>3.6\times10^{-7}$ GeV^{-1}. This result is an empirical fact, but it is of broader interest because of the theoretical prediction for the existence of Nambu-Goldstone bosons [1] discussed in the Introduction. Limits on such nearly massless, weakly coupled particles have also been obtained from atomic physics experiments [35,36] and from the absence of spin-dependent long-range forces [37]. The limits from these laboratory experiments are summarized in Table VII. In this table and hereafter we will express limits in terms of the inverse coupling M, because of its natural interpretation as a symmetry breaking scale. For the data entries in Table VII it is assumed that a pseudoscalar particle couples directly to electrons, an assumption not necessary for the interpretation of our experiment. High-energy experiments [4], on the other hand, can explore the range of massive particles through their direct production and decay into e^+e^-, or because of their absence in certain particle decays, such as $K^+\to\pi^++a$, $J/\psi\to\gamma+a$, and $\Upsilon\to\gamma+a$. The limits established by such experiments are generally in the range $M>10^4$ GeV.

Of all possible low mass particles, the axion has received the most attention as discussed in the Introduction. Astrophysical limits constrain a large fraction of the available phase space in the m_a-$g_{a\gamma\gamma}$ plane [9,10] as shown in Fig. 20. A highly reliable limit comes from the age of the Sun, since axion production in the core would affect the solar lifetime. If axions can carry away energy faster than the nuclear reactions can liberate it, the star would contract to raise its temperature and the nuclear reaction rate. A hotter star has a greater photon (and axion) luminosity, thus accelerating its evolution and shortening its lifetime. From the age of the Sun, Raffelt and Dearborn [38] calculate a limit of $M>4\times10^8$ GeV for a hadronic axion. This is valid for $m_a<1$ keV as the temperature at the center of the Sun is only a few keV. The limit does not apply for axions which interact too strongly ($M\lesssim10^5$ GeV), because in that case the mean free path becomes shorter, and axions cannot carry energy out of the Sun rapidly.

By a similar argument, the evolution of red giant stars is used to set a limit of $M>3\times10^9$ GeV for hadronic axions. A DFSZ axion (with an e-e-a vertex) would so effectively cool the ^{4}He core of the star, by Compton-type processes, as to prevent helium ignition from ever taking place; correspondingly the limit for the DFSZ axion is $M>10^{11}$ GeV [39]. The observation of neutrons from SN 1987A provided new limits on axions, based on the duration of the neutrino pulse [40]. Axions of mass greater than 10^{-3} eV, but less than 2 eV, would have been able to accelerate the cooling of the neutron star and shorten the neutrino burst [41] and are thus excluded. The cooling of the supernova would occur through nucleon-nucleon-axion bremsstrahlung which depends directly on $f_{\rm PQ}/N$ (or equivalently m_a).

Cosmic axion searches place limits on axion couplings under the assumption that the halo dark matter is axion dominated. The microwave cavity experiments [11] place a limit of $M>10^{13}$ GeV for a narrow mass range,

$$4\times10^{-6}\ \text{eV}<m_a<1.5\times10^{-5}\ \text{eV}\ .$$

A recent telescope search looked for relic axions that had condensed in galactic clusters and subsequently decayed into two photons; this search eliminated axions of mass 3–8 eV [42]. An experiment to detect axions emitted from the Sun by converting them to x-ray photons in a magnetic field [43] gives laboratory limits similar to those obtained from the solar lifetime [10]. These results are summarized in Fig. 20 as a function of coupling $g_{a\gamma\gamma}$ and axion mass. The diagonal solid line is the prediction of Eq. (2b) for the relation between $g_{a\gamma\gamma}$ and m_a, assuming $E/N=8/3$ as in grand unified models and is subject to

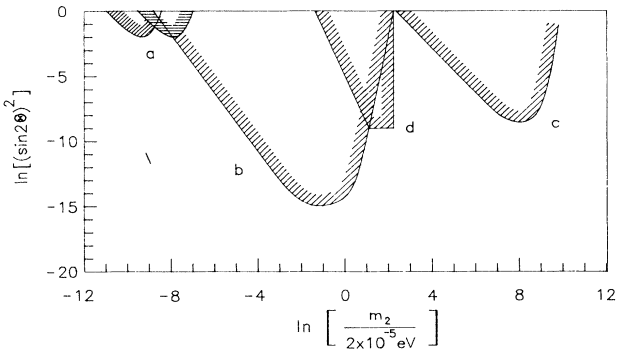

FIG. 19. Constraints on photon mixing obtained from (a) Jupiter's and Earth's magnetic fields; (b) experiments testing the Coulomb law; (c) comparing the Rydberg constant for different atomic transitions; (d) this experiment. For (a)–(c) see Ref. [14]. The excluded regions are shown hatched.

TABLE VII. Limits on the coupling of light pseudoscalars to matter. $g_{aff} \equiv m_f/V, g_{a\gamma\gamma} = 1/M, M \sim V/\alpha$.

Experiment	Limit (GeV)	Interaction	Reference
$J/\psi \to \gamma + a$ $\Upsilon \to \gamma + a$ $K^+ \to \pi^+ + a$	$V > 50$	q-q-a	[4]
$\omega(^{201}\mathrm{Hg})/\omega(^{199}\mathrm{Hg})$	$V > 3\times10^3$	q-q-a /e-e-a	[35]
Superconducting screening	$V > 10^4$	e-e-a	[36]
Long-range spin-dependent force	$V > 50$	e-e-a	[37]
This experiment	$M > 2.8\times10^6$	γ-γ-a	–

the uncertainties discussed in the Introduction. It is important to note that the present experiment and the solar and red giant limits, as well as the microwave experiments are directly related to $g_{a\gamma\gamma}$. On the other hand, the particle decay experiments and the limits from SN 1987A, which are indicated by the two vertical lines in the figure, relate to (f_{PQ}/N) or m_a.

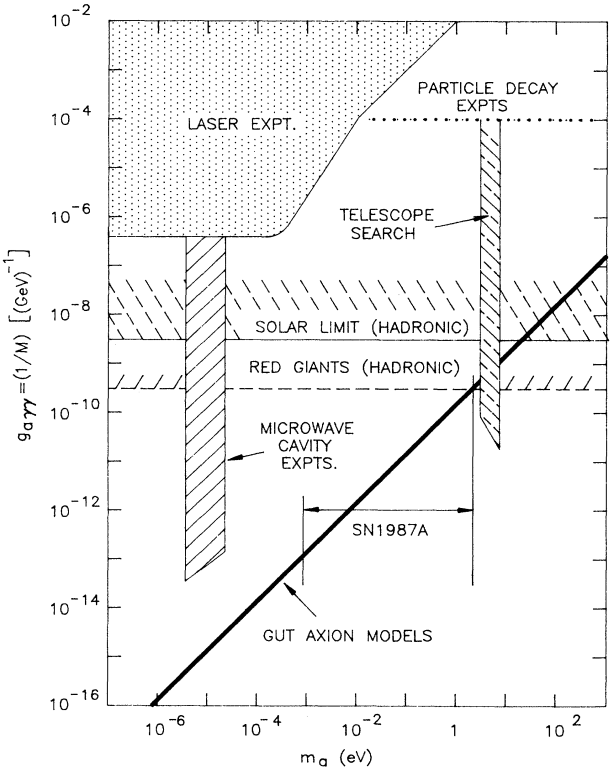

FIG. 20. Limits on axion mass and axion coupling to two photons. Results from this experiment are based on the absence of an optical rotation (for $m_a < 10^{-3}$ eV) and on the absence of ellipticity (for $m_a > 10^{-2}$ eV). The solar limit, red giant limit and the regions excluded by the cosmic axion experiments are also shown. The heavy solid line is the prediction of the relation between m_a and $g_{a\gamma\gamma}$ for axions embedded in GUT's. [See Eq. (2b).] The limit from particle decay experiments is also indicated, and the limits on m_a from SN 1987A are shown as the two vertical lines at $m_a = 2$ eV and 10^{-3} eV.

From a technical point of view, this experiment was made possible by the availability of a suitable laser and of high magnetic fields. It was shown that with the shunt mirror in place the shot noise limit could be reached. However, when the light traveled through the cavity, both random and systematic noise exceeded the shot-noise level. It is possible that these effects could be reduced in the future, but they are inherent at the low modulation frequency imposed by the use of high field superconducting magnets. Stray field and laser alignment stability would also have to be improved in order to reach better sensitivity.

The best sensitivity achieved was 7.6×10^{-9} rad/$\sqrt{\mathrm{Hz}}$, and was maintained for an integration time $T_{\mathrm{int}} = 3.1\times10^4$ s, resulting in an rms noise level of 4.3×10^{-11} rad. From our experience, the maximum useful integration time is 10^5 s. Higher laser power may be used to further reduce the shot-noise limit; this, however, affects the optics, introducing other sources of noise due to thermal stress. Equally important is the motion of the mirrors which follows the modulation of the magnetic field. This seems unavoidable, and can be best corrected by a suitable feedback loop.

The photon regeneration experiment is not subject to the systematic effects that dominate the optical rotation experiment. This is because the former is based on the appearance of light, rather than on the detection of a small perturbation of the incident laser beam. The price for this important advantage is that the observable signal is proportional to $g^4_{a\gamma\gamma}$ rather than to $g^2_{a\gamma\gamma}$ as for the latter experiment. Furthermore, it is difficult to improve the limits on M in the regeneration experiment since M scales as $T_{\mathrm{int}}^{1/8}$. [See Eq. (16b).]

ACKNOWLEDGMENTS

This experiment would not have been possible without the strong support of Brookhaven National Laboratory; we thank in particular D. Lowenstein, S. Ozaki, N. P. Samios, and T. L. Trueman. The cryogenic effort was provided and efficiently maintained by H. Hildebrand and his group, and by R. Meier and his group. Power supply and magnet connections and control were provided by G. Ganetis and his group. Roger Davis and Mike

Caruso are thanked for maintaining the vacuum. Joe Scaduto, Tom Blair, and Al Pendzick were the liaison engineers. Ed Turano, Steve Boege, and Paolo Micossi participated at various stages of data taking. We also thank T. Haelen, P. Borelli, and K. Kubath for mechanical and optical design and construction at the University of Rochester. This work was supported in part by the U.S. Dept. of Energy under Contract Nos. DE-AC02-76CH00016, DE-AC02-76CH03000, and DE-AC02-76ER13065.

[1] Y. Nambu, Phys. Rev. Lett. **4**, 380 (1960); J. Goldstone, Nuovo Cimento **19**, 154 (1961).

[2] L. Maiani, R. Petronzio, and E. Zavattini, Phys. Lett. B **175**, 359 (1986); A. A. Ansel'm, Yad. Fiz. **42**, 1480 (1985) [Sov. J. Nucl. Phys. **42**, 936 (1985)].

[3] R. D. Peccei and H. R. Quinn, Phys. Rev. Lett. **38**, 1440 (1977); Phys. Rev. D **16**, 1791 (1977); see also S. Weinberg, Phys. Rev. Lett. **40**, 223 (1978); F. Wilczek, *ibid.* **40**, 279 (1978).

[4] C. N. Brown *et al.*, Phys. Rev. Lett. **57**, 2101 (1986); A. Bross *et al.*, *ibid.* **67**, 2942 (1991); W. T. Ford *et al.*, Phys. Rev. D **33**, 3472 (1986); H. J. Behrend *et al.*, Phys. Lett. B **176**, 247 (1986); C. Hearty *et al.*, Phys. Rev. Lett. **58**, 1711 (1987); N. J. Baker *et al.*, *ibid.* **59**, 2832 (1987); C. Edwards *et al.*, *ibid.* **48**, 903 (1982); M. S. Alam *et al.*, Phys. Rev. D **27**, 1665 (1983); B. Niczyporuk *et al.*, Z. Phys. C **17**, 197 (1983); M. Sivertz *et al.*, Phys. Rev. D **26**, 717 (1982).

[5] A low mass axion would not lead to a detectable long-range force since the particle is a pseudoscalar, so that the force would be spin dependent. Since in bulk matter the net spin is infinitesimal, there is no net force.

[6] M. Dine, W. Fischler, and M. Srednicki, Phys. Lett. **104B**, 199 (1981); A. R. Zhitnitsky, Yad. Fiz. **31**, 497 (1980) [Sov. J. Nucl. Phys. **31**, 260 (1980)].

[7] J. E. Kim, Phys. Rev. Lett. **43**, 103 (1979); M. A. Shifman, A. I. Vainshtein, and V. I. Zakharov, Nucl. Phys. **B166**, 493 (1980).

[8] J. E. Kim, Phys. Rep. **150**, 1 (1987).

[9] M. S. Turner, Phys. Rep. **197**, 67 (1990).

[10] G. G. Raffelt, Phys. Rep. **198**, 1 (1990).

[11] S. De Panfilis *et al.*, Phys. Rev. Lett. **59**, 839 (1987); W. U. Wuensch *et al.*, Phys. Rev. D **40**, 3153 (1989); C. Hagmann *et al.*, *ibid.* **42**, 1297 (1990).

[12] M. Delbruck, Z. Phys. **84**, 144 (1933).

[13] K. Van Bibber *et al.*, Phys. Rev. Lett. **59**, 759 (1987).

[14] I. Y. Kobzarev and L. B. Okun, Usp. Fiz. Nauk **95**, 131 (1968) [Sov. Phys. Usp. **11**, 338 (1969)]; L. B. Okun, Zh. Eksp. Teor. Fiz. **83**, 892 (1982) [Sov. Phys. JETP **56**, 502 (1982)]; V. V. Popov and O. V. Vasil'ev, Europhys. Lett. **15**, 7 (1991); A. S. Goldhaber and M. M. Nieto, Rev. Mod. Phys. **43**, 277 (1971).

[15] G. Raffelt and L. Stodolsky, Phys. Rev. D **37**, 1237 (1988).

[16] W. Heisenberg and H. Euler, Z. Phys. **38**, 714 (1936); V. F. Weisskopf, Mat. Fys. Medd.-K. Dan Vidensk. Selsk. **14**, 6 (1936); J. Schwinger, Phys. Rev. **82**, 664 (1951); S. L. Adler, Ann. Phys. (N.Y.) **67**, 599 (1971).

[17] G. Jarlskog and L. Jonsson, Phys. Rev. D **8**, 3813 (1973).

[18] J. Bailey *et al.*, Nucl. Phys. **B150**, 1 (1979); J. Calmet *et al.*, Rev. Mod. Phys. **49**, 21 (1977).

[19] Equation (17c) is valid for light propagation in vacuum, since a medium with refractive index n suppresses the oscillations unless the relationship $(n-1)\omega \ll m_2^2/2\omega$ is satisfied.

[20] We used Glan Thompson polarizers purchased from Karl Lambrecht Co., Chicago, IL.

[21] Colliding Beam Accelerator, E. J. Bleser *et al.*, Nucl. Instrum. Methods A **235**, 435 (1985).

[22] The magnets were originally designed for a ramping rate of 8 A/s.

[23] D. Herriott, H. Kogelnik, and R. Kompfner, Appl. Opt. **3**, 523 (1964); H. Kogelnik and T. Li, Proc. IEEE **54**, 1312 (1966); D. Herriott and Harry J. Schulte, Appl. Opt. **4**, 883 (1965).

[24] The LPC was manufactured by Cambridge Research and Instrumentation.

[25] W. Schottky, Ann. Phys. (Leipzig) **57**, 541 (1918); A. van der Ziel, *Noise: Sources, Characterization, Measurement* (Prentice-Hall, Englewood Cliffs, NJ, 1970).

[26] For more details, see R. E. Cameron, "Search for new photon couplings in a magnetic field," Ph.D. thesis, University of Rochester (1992), Report No. UR-1262.

[27] PZL-030 from Burleigh Instruments Inc., Fischers, NY.

[28] Hamamatsu S1557.

[29] A. D. Buckingham, W. H. Prichard, and D. H. Whiffen, Trans. Faraday Soc. **63**, 1057 (1967).

[30] R. Cameron *et al.*, J. Opt. Soc. Am. B **8**, 520 (1991).

[31] R. Cameron *et al.*, Phys. Lett. A **157**, 125 (1991).

[32] Y. K. Semertzidis *et al.*, Phys. Rev. Lett. **64**, 2988 (1990).

[33] It is possible that the mirror motion follows dB/dt in which case the false signal would be orthogonal to the magnet phase.

[34] G. Ruoso *et al.*, Z. Phys. C **56**, 505 (1992).

[35] E. B. Aleksandrov *et al.*, Zh. Eksp. Teor. Fiz. **85**, 1899 (1983) [Sov. Phys. JETP **58**, 1103 (1983)].

[36] P. V. Vorobyev and Ya. I. Gitarts, Phys. Lett. B **208**, 146 (1988).

[37] J. K. Hoskins, R. D. Newman, R. Spero, and J. Schultz, Phys. Rev. D **32**, 3084 (1985).

[38] G. G. Raffelt and D. S. P. Dearborn, Phys. Rev. D **36**, 2211 (1987).

[39] D. S. P. Dearborn *et al.*, Phys. Rev. Lett. **56**, 26 (1986).

[40] K. Hirata *et al.*, Phys. Rev. Lett. **58**, 1490 (1987); R. M. Bionta *et al.*, *ibid.* **58**, 1494 (1987).

[41] M. S. Turner, Phys. Rev. Lett. **60**, 1797 (1988); R. Mayle *et al.*, Phys. Lett. B **203**, 188 (1988); **219**, 515 (1989).

[42] M. A. Bershady *et al.*, Phys. Rev. Lett. **66**, 1398 (1991).

[43] D. M. Lazarus *et al.*, Phys. Rev. Lett. **69**, 2333 (1992); such an experiment is also in progress at the Institute for Nuclear Physics, Novosibirsk, Russian Republic [P. Vorobyev (private communication)].